THE ASSEMBLY HISTORY OF THE MILKY WAY STELLAR HALO

by

Shobhit Steven Kisku

A thesis submitted in partial fulfilment for the
degree of Doctor of Philosophy

January 15, 2024

Declaration

The work presented in this thesis was carried out at the Astrophysics Research Institute, Liverpool John Moores University. Unless otherwise stated, it is the original work of the author.

While registered as a candidate for the degree of Doctor of Philosophy, for which submission is now made, the author has not been registered as a candidate for any other award. This thesis has not been submitted in whole, or in part, for any other degree.

Shobhit Steven Kisku
Astrophysics Research Institute
Liverpool John Moores University
IC2, Liverpool Science Park
146 Brownlow Hill
Liverpool
L3 5RF
UK

January 15, 2024

Abstract

The Milky Way as a galaxy is one that holds particular interest to me because it is the one in which we exist. Understanding the origins of the Galaxy is key to figuring out our importance in the Universe and whether there is a purpose for our existence or whether we are merely a series of accidents. Being able to study the Milky Way from such a close distance, since we are in it, allows us to analyse its different components on a star-by-star basis. The stellar halo, in particular, due to the large dynamical timescales, yields the most information about the early stages of the Galaxy. This large dynamical timescale means that sub-structures in the Milky Way halo are preserved. By understanding the formation history of our own Galaxy, we can place constraints on the formation of other disc galaxies. And knowledge of the formation history of other galaxies lets us place the Milky Way in a larger context and gets us closer to answering the question: *do we live in a special place in the Universe?* This thesis aims to provide insight into the formation history of the Galaxy, achieved through the analysis of some of its sub-structures.

Recent evidence based on APOGEE data for stars within a few kpc of the Galactic Centre suggests that dissolved globular clusters contribute significantly to the stellar mass budget of the inner halo. I enquire into the origins of tracers of globular cluster dissolution, N-rich stars, that are located in the inner 4 kpc of the Milky Way. From an analysis of the chemical compositions of these stars, I establish that about 30 per cent of the N-rich stars previously identified in the inner Galaxy may have an accreted origin. This result is confirmed by an analysis of the kinematic properties of my sample. The specific frequency of N-rich stars is quite large in the accreted population, exceeding that of its in situ counterparts by near an order of magnitude, in disagreement with predictions from numerical simulations. We hope that our numbers provide a useful test to models of globular cluster formation and destruction.

The heated disc of the Galaxy, known as the Splash, has been predicted and recently discovered due to its halo-like kinematics and disc-like chemistry. Using data from APOGEE and *Gaia*, I examine the spatial and chemodynamical properties of the Splash compared to the disc. In addition, I analyse the Splash population of Milky Way-like galaxies in the `ARTEMIS` simulations, comparing galaxies with Gaia Enceladus/Sausage (GE/S)-like mergers and those without. The analysis performed reveals a statistically significant chemical difference between the Splash and the disc, showing that the Splash is an older population with a shorter period of star formation. I also find a smooth correlation in the high-α population of both the Milky Way and simulated galaxies, regardless of if they've undergone a GE/S-like merger, when comparing α-abundance to kinematics. Finally, a simple comparison of the Splash fraction of the galaxies reveals that even galaxies with only minor mergers can create a Splash comparable to galaxies with GE/S-like mergers. I conclude that while a GE/S-like merger is shown to cause a Splash, it is not necessary. The orbital direction of the accreted population is what also plays a big role in creating a Splash.

The above results place constraints on our understanding of the effects of mergers on the stellar populations in the Milky Way. From discovering the existence of accreted globular cluster members, leading to the question of whether the environment of dwarf galaxies can cause the destruction of globular clusters, to understanding how a merger affects the disc of the Galaxy and comparing the results of this interaction in different Milky Way-like simulated galaxies. The findings of this thesis pave the way for future works towards the goal of fully reconstructing the formation history and evolution of the Milky Way and placing it in a larger context to better understand and compare it with other galaxies.

Shobhit Steven Kisku January 15, 2024

Publications

During the course of the preparation of this thesis, the work within Chapters 2, has been presented in the following jointly authored publications:

1 *'An enquiry on the origins of N-rich stars in the inner Galaxy based on APOGEE chemical compositions'*
Kisku, Shobhit., Schiavon, Ricardo P., Horta, Danny., Mason, Andrew., Mackereth, J Ted., Hasselquist, Sten., García-Hernández, D. A., Bizyaev, Dmitry., Brownstein, Joel, R., Lane, Richard, R., Minniti, Dante., Pan, Kaike., Roman-Lopes, Alexandre., MNRAS, Volume 504, Issue 2.

Publication 1 forms the basis of Chapter 2, and is based on studying N-rich stars in the inner Galaxy using APOGEE DR16 and *Gaia* DR2 data. All analysis was carried out by S. Kisku, with intellectual input from R. P. Schiavon, and D. Horta. The original manuscript was prepared by S. Kisku, with an important contribution from R. P. Schiavon, and minor comments from co-authors, colleagues and an anonymous referee were incorporated later.

Acknowledgements

A huge amount of thanks goes to my supervisor, Ricardo Schiavon. From the start and through to the end of the PhD, you have always been there to guide me whenever I needed it. You have been a great mentor and your positive attitude and kindness are highly respected. Thank you very much.

I would also like to thank my second supervisor, Andreea Font. We did not get to work together as much as I would have liked, but you have always been available to assist whenever required.

To the Milky Way team, you're all awesome. Danny Horta, without you, the last 4 years would have been a struggle. You consistently checked in on me, you were always there when I needed help or if I needed someone to talk to. I cannot thank you enough. Ted Mackereth, thank you for all the insightful conversations. Whenever another perspective was needed, you were there. Andrew Mason, my brother, we've been through this whole journey together. Thank you for being a great friend and supporting me throughout.

I extend my gratitude to all the staff and colleagues for making the ARI a welcoming and friendly environment. In particular, thank you to all the friends in Room 3.18: Adrian, Andrew, Bethan, Flo, Jemima, Kyle, Phoebe, Sarah, Stephen and Tutku. You are all beautiful people.

Most importantly, I thank my parents and brother for all their love and support. I am incredibly grateful for everything you have done for me and for providing me with all the necessities. And finally, to my other half, Rosetta, thank you for all your support and much-needed motivation!

“Many Things That Seem Threatening In The Dark Become Welcoming When We Shine Light On Them”

– Uncle Iroh

Contents

List of Figures

List of Tables

. . .

Chapter 1

Introduction

In our search to understand how the world we live in works, we must first understand how it came about. Humans have always been curious about what lies beyond the Earth, with early studies of the Universe taking us as far back as ancient Greece and BCE India. At these times it was common to believe that the Earth was at the centre of the Universe with everything else spinning around it. It was not until the 16th century that the heliocentric model was presented by Copernicus, placing the Sun at the centre of the Universe. In fact, in our current understanding of cosmology, not even the Sun, our solar system, or the Milky Way is placed at the centre of the Universe. This raises the question; *do we live in a special place in the Universe?*

To study the large-scale structure of the Universe, we must look to the greatest contributor to the Universe that we can detect. The building blocks of the Universe consist of three things: dark energy, dark matter and baryonic matter. Knowing how all of these components of the Universe interact to form galaxies, stars, planets and all other things is crucial to understanding how we got to be here. Since only baryonic matter is able to be directly detected, it makes it an ideal tracer to study the Universe.

Our Universe hosts an immensely large number of galaxies, on the order of hundreds of billions just in the observable region. Of all these galaxies there is one that holds the most information that we can access, home to humanity, and a personal favourite, our Galaxy, the Milky Way.

The fundamental question of how the Galaxy was formed is what defines Galactic Archaeology. The idea of using long-lived stars in various stellar components of the Milky Way to uncover its history is much like how archaeologists use fossils or artefacts to learn about the past. The benefit of studying the Milky Way to date has been the ability to obtain data for individual stars within it to a high degree of resolution, allowing

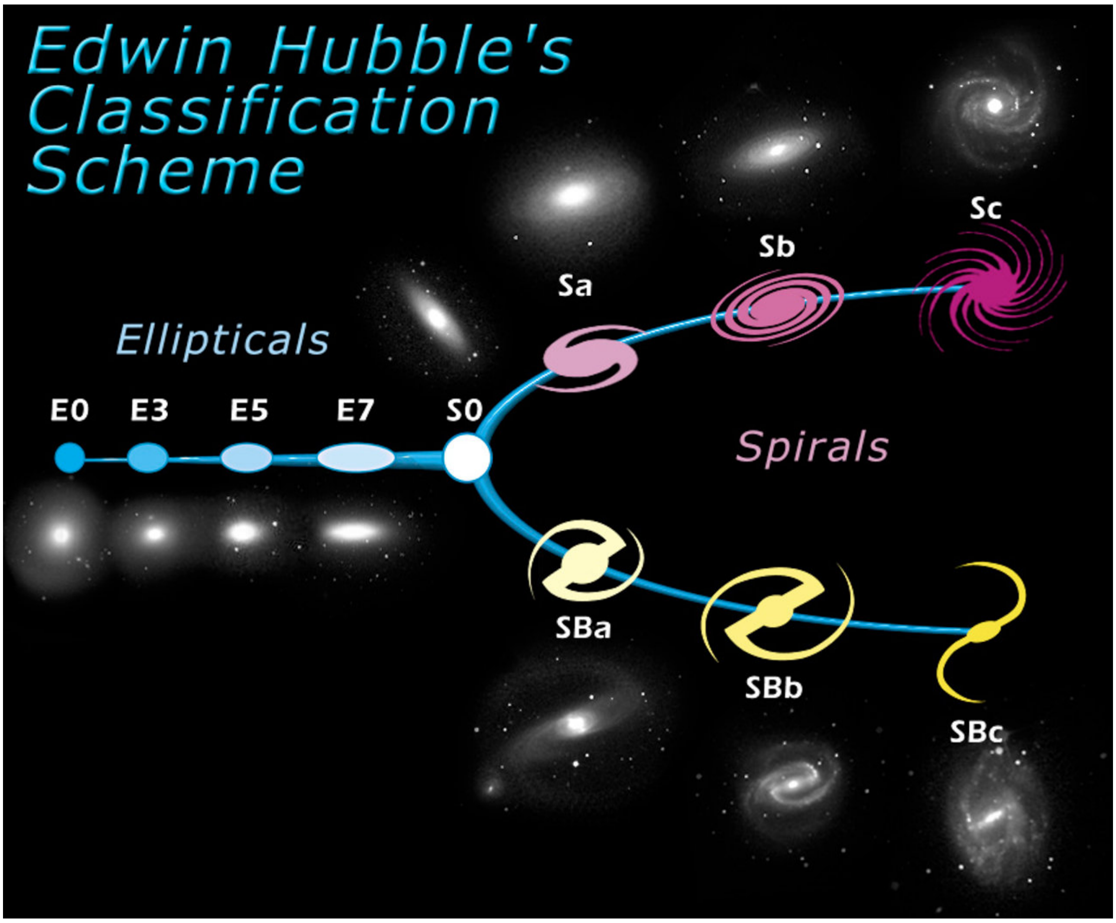

FIGURE 1.1: The Hubble tuning fork diagram - Image Credit: NASA & ESA

for detailed photometric and spectral data on a star-by-star basis. Studying the Milky Way in such detail allows us to test current galaxy formation models. This, however, relies on whether the Milky Way is a typical galaxy in terms of its characteristics (e.g. mass, shape and size). If the Milky Way is somehow *atypical* in its assembly history, distribution of stellar populations, chemodynamical properties, or any other properties when compared to galaxies sharing similar characteristics, then knowing where it lies in comparison to other galaxies will help us better understand whether our existence in the Universe is special.

1.1 The Milky Way

Until the 20th century, our Galaxy was thought to encompass the whole universe. When looking up at the night sky, all the bright points were assumed to be stars within the Milky Way. It wasn't until 1926 when Edwin Hubble showed that our Galaxy is only one of many others (Hubble, 1926). Since this work, we have been able to characterise galaxies and see where the Milky Way lies in the larger context.

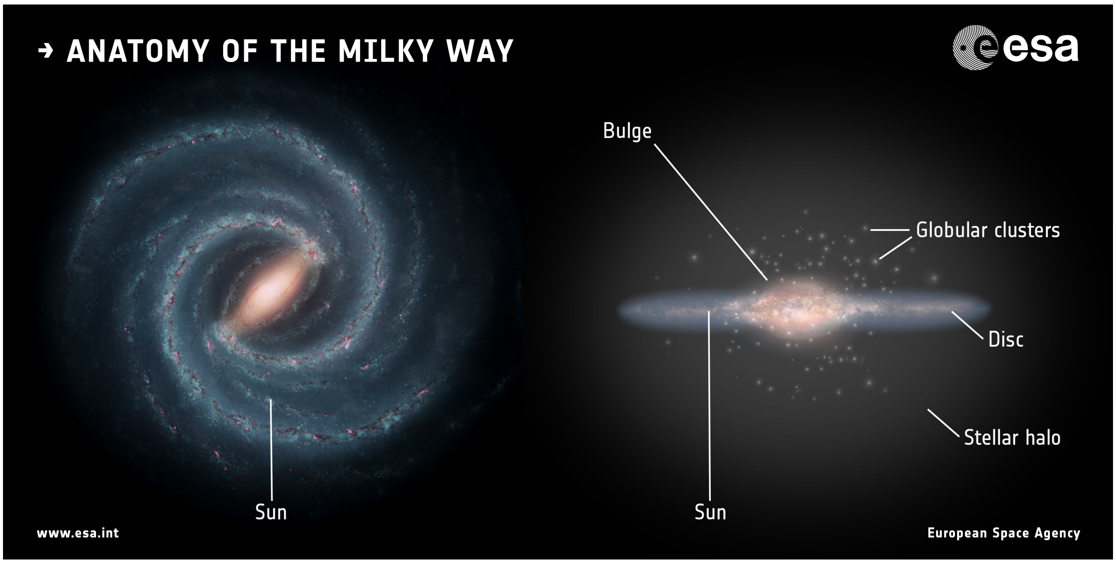

FIGURE 1.2: Artist's impression of the Milky Way galaxy and its components - Image Credit: *left*: NASA/JPL-Caltech; *right*: ESA; *layout*: ESA/ATG medialab

For a while, and to this day, galaxies are largely classified by their morphology. Most galaxies fall under one of two types: elliptical or spiral. With more observations, this classification was extended to include finer details, leading to Hubble's tuning-fork diagram[1], See Figure 1.1. In this diagram, the Milky Way is classified as a barred-spiral (specifically an SBc Gerhard, 2002). We can also look at other properties of galaxies, for example, their colour and magnitude. In the colour-magnitude diagram, most galaxies fall into either the 'red sequence', where star formation has been largely quenched, or the 'blue cloud', with ongoing star formation, with the 'green valley' in between, where the Milky Way resides (Mutch et al., 2011).

The morphology of the Milky Way[2] (Figure 1.2), as mentioned above, is well-established to be characterised by the presence of an extended disc, with multiple spiral arms, a bulge/bar and a diffuse stellar halo. Some of the precise details of these components are difficult to discern, such as the inner regions given the dusty nature of the disc and our position within it and the low density of the stellar halo compared to that of the stellar disc. The Galaxy is estimated to have a stellar component with a mass on the order of $6.43 \times 10^{10} \mathrm{M}_\odot$ (McMillan, 2011) extending out to 25-30 kpc, and a dark matter halo component on the order of $\sim 10^{12} \mathrm{M}_\odot$ (See Bland-Hawthorn & Gerhard (2016) and references therein) and the edge at ~ 290 kpc (Deason et al., 2020).

---

[1] `https://esahubble.org/images/heic9902o/`

[2] `https://sci.esa.int/s/WmQpGLW`

1.1.1 The Inner Galaxy & Bulge/Bar

The inner regions of galaxies are characterised as having a higher density. In the Milky Way, this region was initially thought to be a single component. However, the latest data shows it to be an overlap of the different components in the Galaxy: the thick/thin discs, the stellar halo, and the bulge and bar. The Inner Galaxy hosts some of the oldest stars (Bovy et al., 2019; Queiroz et al., 2021) spanning a metallicity range as low as [FE/H] ~ -4.0 (Youakim et al., 2020) and as high as [FE/H] ~ 0.6 (Ness et al., 2013). Since the Inner Galaxy is a superposition of different stellar systems, going from high-α at low metallicities to low-α at high metallicities, it is shown to host at least five populations (Horta et al., 2021a). In comparison to the rest of the stellar components of the Milky Way disc, the Inner Galaxy is shown to be chemically less evolved (Bovy et al., 2019), however, a more recent study by Eilers et al. (2022) shows that on average the Inner Galaxy is more evolved (more metal-rich). The discrepancy observed between these two findings is due to a correction made by the latter accounting for the systematic effects of APOGEE. On top of consisting such a wide range of populations, it is the innermost regions that have the highest density of halo stars (Horta et al., 2021b).

A unique component of the Inner Galaxy is the bulge. Bulges are mostly visible in larger, more massive, galaxies like our own Milky Way. The formation of the bulge was believed to be built through mergers during the very early stages of the Galaxy's formation, the so-called *'classical'* bulge. However, near-infrared photometry from the COBE satellite was the first to establish the boxy nature of the bulge (Weiland et al., 1994; Binney et al., 1997), which was later confirmed by the `2MASS` star count map (Skrutskie et al., 2006). Recent star count data have established that the bulk of the bulge stars are part of a box/peanut (b/p-bulge) structure representing the inner part of the Galactic bar (Wegg & Gerhard, 2013). Though the existence of a classical bulge is still debated (Nataf, 2017; Barbuy et al., 2018)

Red Clump Giants (RCGs) are representative of most of the bulge stars (Bland-Hawthorn & Gerhard, 2016; Ness et al., 2013). RCGs reveal a strong off-centred X-shape structure, as is seen in a sample of galaxies from Bureau et al. (2006); see also Nataf et al. (2015). Such X-shaped structures are thought to be a consequence of instabilities in the disc giving rise to the b/p morphology (based on studies of N-body simulations, e.g. Athanassoula, 2005; Debattista et al., 2006).

Most of the stars in the bulge are in a rotating triaxial structure, the Galactic bar, which has a major axis in the first Galactic quadrant ($0° < l < 90°$). The angle between the major axis and the Sun-Galactic centre is found to be $27° \pm 2°$ (Wegg & Gerhard, 2013) consistent with earlier determinations (20°-35°, Dwek et al., 1995; Binney et al., 1997;

Stanek et al., 1997; Freudenreich, 1998; Bissantz & Gerhard, 2002; López-Corredoira et al., 2005; Rattenbury et al., 2007; Cao et al., 2013). With the advent of the *Gaia* satellite (Gaia Collaboration et al., 2016), Bovy et al. (2019) have further constrained this value to the current estimate of $\sim 25°$. They also show, using the latest survey data, that the bar of the Milky Way has a length of approximately ~ 10 kpc and is rotating at ~ 41 km/s kpc^{-1} (see also Portail et al. (2017) and Sanders et al. (2019)).

The innermost regions are where we expect to find the oldest stars that were born in the Galaxy (Tumlinson, 2010; Starkenburg et al., 2017; Arentsen et al., 2020), making it an interesting region to study the history of the Milky Way.

1.1.2 The Disc

The disc of the Milky Way amounts to a mass of $3.6 - 5.4 \times 10^{10} M_\odot$ (Flynn et al., 2006). The main distinguishing feature of the Galactic disc is the spiral structure, with either 2 or 4 spiral arms (Drimmel, 2000). Additionally, the disc is understood to be a construction of two components, referred to as the 'thick' and 'thin' disc. The Sun is located in the Orion spiral arm, approximately ~ 8.178 kpc from the Galactic centre (GRAVITY Collaboration et al., 2019) and roughly ~ 0.02 kpc above the midplane (Bennett & Bovy, 2019). Trying to observe distant regions of the disc comes with the difficulty of source confusion and interstellar extinction, leaving unknowns in our complete understanding of the disc.

The two components of the disc are referred to as thick and thin due to their exponential scale heights, z. A large survey of M dwarfs in the solar neighbourhood by Jurić et al. (2008) finds $\mathrm{z}^{\mathrm{t}} \approx 300$ pc for the thin disc and $\mathrm{z}^{\mathrm{T}} \approx 900$ pc for the thick disc. The disc can also be separated into two components based on their chemistry, referred to as the high- and low-α. The high-/low-α definition of the disc is similar to the geometrically defined thick/thin disc, with the low-α disc having a scale height of ≈ 0.2 kpc and the high-α having a scale height of ≈ 1 kpc (Bovy et al., 2012, 2016). The two components of the disc are believed to have evolved independently from each other, with age measurements of the discs revealing the low-α disc to be younger than the high-α disc. This is also shown by the metallicity distribution of the low-α disc being weighted towards higher metallicity stars than that of the high-α disc. As is hinted by the name, the high-α disc consists of higher α-abundances, e.g. Mg, Si, Ca. The α-element distribution of the disc at fixed [Fe/H] is bimodal (Mackereth et al., 2017).

There has been much research into the properties of the high-α disc. The high-α disc is easily identifiable in the [Mg/Fe]-[Fe/H] plane as a high density of stars with high Mg stretching a wide range of metallicity. The lower limit of the high-α metallicity distribution function is difficult to discern due to the overlap with halo stars. According to APOGEE, the upper limit of high-α MDF ranges above solar to about [Fe/H] ~ 0.6. It also shows a prominent α-Fe knee at [Fe/H] ~ -0.5 (Hayden et al., 2015). This feature is thought to initially form after the onset of SNe Ia when the contribution to chemical enrichment by SNe Ia becomes comparable to that by SNe II. A new interpretation of the knee is presented by Mason et al., in prep on the basis of an analysis of the EAGLE cosmological numerical simulations.

An interesting component of the high-α disc is the heated thick disc (Font et al., 2011; McCarthy et al., 2012). This component has been identified by various groups and is the focus of the study covered in Chapter 3. The heated disc, also referred to as the Splash (Belokurov et al., 2020), is believed to be the result of the merger of the Galaxy with Gaia-Enceladus/Sausage (GE/S). That merger, which was a head-on collision, caused the old stars in the thick disc to scatter out into the halo, resulting in a kinematically halo-like substructure with disc-like chemistry.

1.1.3 The Stellar Halo

Making up only a tiny fraction of the total stellar mass of the Milky Way, the stellar halo is arguably the most important component of the Galaxy when it comes to understanding the early history of the MW formation. This region of the Galaxy provides a wealth of information about its history due to the long dynamical timescales compared to the disc or bulge. Longer dynamical timescales allow for the preservation of sub-structures such as stellar debris of smaller satellite systems (streams, dwarf galaxies and globular clusters) that reside in the halo. These sub-structures are the result of accretion due to mergers and tidal disruptions of clusters. Studying these structures, especially those which have been residing in the halo since the early formation of the Galaxy, provides vital information about how the Galaxy formed and what processes led to its current state giving us a complete picture of the formation of the Galaxy.

In 1962, Eggen et al. (1962) proposed the first modern formation scenario for the Galactic halo, the ELS model. By measuring the eccentricity and angular momentum of 221 dwarf stars in a model galaxy, they find that stars with the largest ultraviolet excess (lowest metal abundances) are moving in more elliptical orbits. This correlation between the metallicity and orbital energy of a star is discussed in terms of the dynamics of a collapsing galaxy. It is postulated that the initial gas from which a galaxy forms is metal-poor. The collapse of this gas formed the first generation of stars. The gas continues to collapse in both the radial and vertical directions with the radial collapse eventually stopping due to rotation. As the vertical collapse continues, forming a thin disc, the increase in density increases the rate of star formation. The death of first-generation stars as supernovae scatter metals throughout the disc of the galaxy, enriching the gas from which the next generation of stars form.

Some years later, an alternative formation scenario was proposed by Searle & Zinn (1978). In this work, a new method of determining abundances was applied to a sample of red giants in 19 globular clusters that were mostly at a galactocentric distance larger than 8 kpc. They found that the metallicities for these outer clusters are independent of galactocentric distance and that they have a broad spread in the colour of the horizontal branch. This is in contrast to more tightly bound clusters which show very little dispersion in the colour of their horizontal branch. Given these properties, the authors conclude that the loosely bound clusters in the outer halo have a broader range of ages compared to the more tightly bound clusters. If the collapse of gas happens very rapidly, as is suggested by Eggen et al. (1962), taking only a few times 10^8 years to attain circular orbit, and the initial collapse must have been around 10^{10} years ago, around the age of the oldest stars, then these two conditions mean that we would not expect to see younger clusters in the halo of the Galaxy. Searle & Zinn (1978) propose that the gas from which the younger clusters in the outer halo formed must have continued to fall into the Galaxy even after the collapse of its central regions. They also suggest that the interactions of the infalling gas must have dissipated much of its kinetic energy giving rise to transient high-density regions in which stars and clusters can form. These regions then dispersed even while undergoing chemical evolution and the stars and clusters which formed within them eventually fell into dynamical equilibrium with the Galaxy, constituting its present outer halo. The gas which was lost from these protogalactic star-forming regions eventually swept into the Galactic disc.

Roughly speaking, the modern understanding of the early phases of the Milky Way formation is a mixture of the two ideas. Lambda CDM theory explains the large-scale structure of the Universe and how the large potential wells of dark matter halos are the regions where Galaxies are mostly formed (White & Rees, 1978) by the process of hierarchical mass assembly, however, our understanding of Galaxy formation on the smaller scales is still incomplete. Building on the early works mentioned above, we have seen great advances in our knowledge of the Galactic halo over the last few decades. Given the difficulty in observing the distant stellar halo, most of our knowledge comes from observing stars within roughly 20 kpc of the Galactic centre and more so from observations of the solar neighbourhood. We have discovered many substructures such as the Sagittarius dwarf spheroidal (Ibata et al., 1994), an infalling satellite galaxy merging with the Milky Way, and many halo stellar streams (Helmi et al., 1999; Ibata et al., 2016; Belokurov et al., 2018; Martin et al., 2022). In more recent times this field has expanded immensely due to the large amount of data that is being collected. This has resulted in the discovery of many more substructures in the halo of the Milky Way (Belokurov et al., 2006; Schiavon et al., 2017a; Helmi et al., 2018; Haywood et al., 2018; Belokurov et al., 2018; Mackereth et al., 2019; Naidu et al., 2020; Horta et al., 2021a. One of these substructures is of particular interest, Gaia-Enceladus/Sausage (GE/S, Helmi et al., 2018; Belokurov et al., 2018). GE/S is the dominant structure we see in the halo, believed to be the remnants of a dwarf galaxy that merged with the Milky Way about 10 Gyr ago. A piece of early evidence for this structure was found by Brook et al. (2003). It is also believed that this merger event is what caused the Splash. We test this theory in Chapter 3.

1.2 Globular Clusters

Globular clusters (GCs) are highly dense systems containing on the order of a hundred thousand stars that are gravitationally bound. A typical GC is approximately spherical in shape with a half-light radius of a few pc and spanning a mass range of about $10^4 - 10^6$ $M_\odot$. The origins of these systems is yet to be fully understood, yet they provide us with a wealth of information about the nature of the Galaxies in which they reside. Given that GCs are some of the brightest bodies visible, we are able to detect and study them in external galaxies in integrated light. Even within our own Galaxy, where we can resolve individual stars within these systems, GCs have provided us with information such as their ages, chemical compositions and orbital properties, giving us more insight into the formation history of the Milky Way (Searle & Zinn, 1978; Salaris & Weiss, 2002; Massari et al., 2019; Kruijssen et al., 2019; Horta et al., 2020; Forbes, 2020; Callingham et al., 2022). Since these systems are one of the first to form, the ages of *in situ* GCs can also be used as a lower limit for the age of the Galaxy.

The Milky Way hosts about 157 objects classified as GCs (Harris, 2010), extending out to the edges of the Galaxy, which are home to some of the oldest stars in the Galaxy. The age metallicity relation (AMR) of Galactic GCs is shown to bifurcate (Marín-Franch et al., 2009; Forbes & Bridges, 2010; Leaman et al., 2013), with one branch at old ages covering a large range of metallicities and a branch that covers a wider range of ages. The former is believed to trace the GCs formed *in situ* and the latter accreted. This interpretation of the data is also backed up by looking at the Galactocentric distance at which these GCs lie. The old GCs at high metallicity have smaller Galactocentric radii than the others (Kruijssen et al., 2019)

GCs also contribute to the total stellar halo mass budget, around 27.5% at 1.5 kpc and around 4.2% at 10 kpc from the Galactic centre (Horta et al., 2021b). The leading formation scenario proposes that *in situ* GCs were born in very high-density regions and later destroyed due to tidal interactions such as tidal shocks, evaporation and the so-called 'cruel cradle effect' (Gnedin, 2001; Elmegreen, 2010; Kruijssen et al., 2011). We can observe the destruction of such GCs as tidal streams, for example in Pal 5 (Odenkirchen et al., 2003; Phillips et al., 2022). However, some GCs are destroyed beyond the stage of having tidal streams. The stars lost from these GCs are mixed with the field of the halo stars. To detect these dissolved GC members we can use 'chemical tagging' (Freeman & Bland-Hawthorn, 2002). This is a method which uses very detailed and accurate chemical compositions of stars to associate abundance patterns with a star-forming unit. By analysing these patterns, it becomes possible to trace them back to a common origin. Provided that every star-forming unit was chemically unique, a distinction between every single star-forming unit could be made given a large number of elemental abundances. This is, however, observationally very costly. A less expensive method makes use of a smaller number of elemental abundances to associate abundance patterns not with a unique star-forming unit but rather with a stellar population. This less expensive method is called '*weak chemical tagging*' (Schiavon et al., 2017a).

GCs were traditionally thought to be simple stellar systems containing stars of similar age and chemical abundance. In recent times, it has become clear that GCs in fact host multiple stellar populations with wide spreads in ages and abundance (see Bastian & Lardo, 2018, for a review). Most GCs display light element abundance variations (Figure 1.3). The stars with these variations are called second generation GC members. These distinct abundance patterns in stars can be used to identify destroyed GC members (Martell & Grebel, 2010; Lind et al., 2015; Martell et al., 2016; Schiavon et al., 2017a; Koch et al., 2019; Fernández-Trincado et al., 2019; Tang et al., 2019, 2020; Horta et al., 2021b). On the other hand, the first generation GC members are indistinguishable from the field population. Since the early work of Tremaine et al. (1975), all GC formation models are in agreement that GCs have been destroyed at a ~ 97 % level (Gnedin et al., 2014). Identifying destroyed GC members can help solve the mass budget problem (Renzini, 2008), which deals with the lack of first generation stars required in order to synthesise light elements to form the observed number of second generation stars in GCs. This is the focus of the study in Chapter 2, where I identify N-rich stars (second generation GC members) in the inner Galaxy to constrain their origin.

1.3 Summary and thesis outline

Thus far I have given an overview of the field of Galactic Archaeology, starting with the philosophical motive behind why we study the Universe in which we live and how studying our own Galaxy can get us closer to answering the question; *do we live in a*

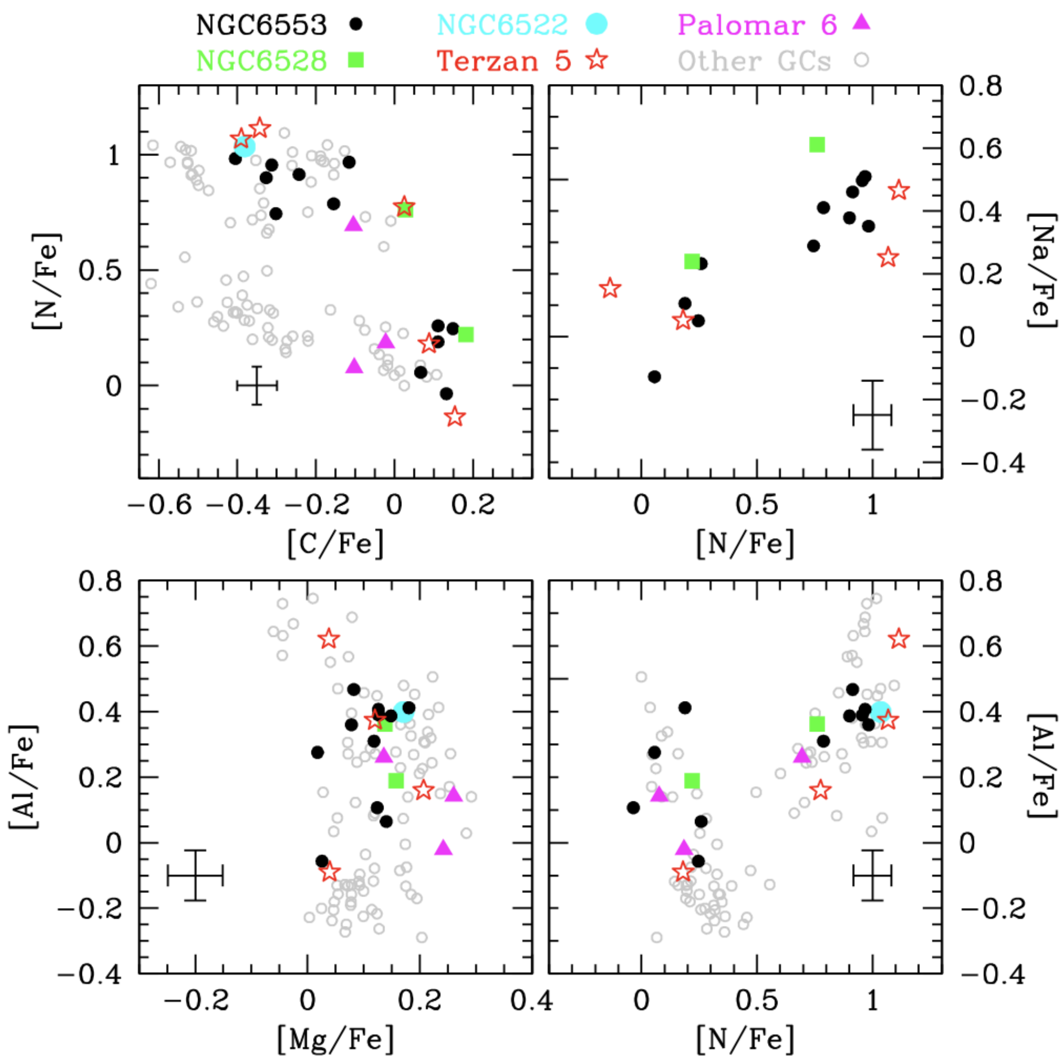

FIGURE 1.3: GCs on various abundance planes displaying light element abundance variations. Figure taken from Schiavon et al. (2017b).

special place in the Universe? I then describe the structure of the Milky Way and its components with the main focus on the three largest components: the bulge/bar, the disc and the stellar halo. Given the complexity and the vast amount of information the stellar halo is able to provide, I dive deeper into its accretion history given our current understanding. I also give a brief background to globular clusters, with a focus on the destroyed members.

In the following chapters, I describe the work I have done to further our understanding of the Milky Way on the basis of cutting-edge observational data and state-of-the-art cosmological simulations. In detail:

- In Chapter 2, I present the results obtained by studying N-rich stars in the inner Galaxy to better constrain their origin and provide a test for GC formation models.

- In Chapter 3, I examine in detail what is claimed to be the heated disc of the Milky Way, dubbed the Splash. I present its chemodynamical properties and compare them to simulations as a test of the leading model for its formation.

Following the main chapters, I present the conclusions of the thesis and future works which will help constrain our understanding of the formation history and evolution of the Galaxy.

Chapter 2

Origin of N-rich stars

2.1 Introduction

One of the main consequences of the current cosmological paradigm, Lambda Cold Dark Matter (Λ-CDM), is that galaxies grow through the process of hierarchical mass assembly, whereby smaller galaxies are accreted to form larger more massive systems. Such theoretical predictions are in line with the identification of phase-space substructures residing in the Galactic stellar halo, such as Gaia-Enceladus/Sausage (GE/S, Belokurov et al., 2018; Haywood et al., 2018; Helmi et al., 2018; Mackereth et al., 2019) and Sequoia (Myeong et al., 2019). As well as halo stellar streams (Helmi et al., 1999; Ibata et al., 2016; Belokurov et al., 2018) and ongoing accretion, such as the Sagittarius dwarf spheroidal (Sgr dSph, Ibata et al., 1994). The longer dynamical timescales of less dense regions, such as the outer halo, preserve phase-space information and therefore allow the reconstruction of the integrals of motion (IOM) of these accreted systems. The situation is not as simple in the inner halo due to the shorter dynamical timescales. Moreover, large extinction towards the inner Galaxy and crowding by more massive metal-rich Galactic components, such as the thick and thin disc, and the bar, make observational access to the inner halo difficult. These difficulties have recently been overcome by the APOGEE survey (Majewski et al., 2017), which obtained detailed chemistry based on NIR spectroscopy for over 10^4 stars in the inner Galaxy, leading up to the discovery of a large population of N-rich stars within a few kpc of the Galactic centre, and the recent identification of Heracles (Horta et al., 2021a).

In addition to the phase-space substructure, stellar streams and ongoing accretion events in the Galactic stellar halo, ancient Globular Clusters (GC) are also thought to contribute relevantly to the total stellar halo mass budget (Martell et al., 2016; Schiavon et al., 2017a; Koch et al., 2019; Reina-Campos et al., 2020; Hughes et al., 2020; Horta et al., 2021b). Such contribution arises from the dissolution and/or evaporation of GCs, which are disrupted via different processes (e.g. tidal shocks, evaporation and disruption by encounters with massive molecular clouds, Gnedin, 2001; Elmegreen, 2010; Kruijssen et al., 2011) so that stars resulting from GC dissolution can be found in the field of the stellar halo.

Detection of the remnants of GC dissolution in the field is made possible by the presence of stars with chemically peculiar chemical compositions in GCs. These systems have been found to host multiple stellar populations with distinct abundance patterns (for a detailed description, see a review by Bastian & Lardo, 2018). Stars that display the same abundance patterns as the field population are dubbed "First Generation" (FG) stars, whereas those that show enhancements in He, N and Na, and show lower O and C are referred to as "Second Generation" (SG) stars. Since abundance patterns of FG stars are indistinguishable from those of field populations, stars with abundance patterns typical of SG population are used as tracers of the contribution of dissolved GCs to the stellar mass budget of the Galaxy.

Field stars that display abundance patterns typical of SG GC stars have been identified in the stellar halo by several groups (Martell & Grebel, 2010; Lind et al., 2015; Martell et al., 2016; Koch et al., 2019; Tang et al., 2019, 2020). Using APOGEE DR12 data, Schiavon et al. (2017a) identified a large population of N-rich stars in the inner ∼2-3 kpc from the Galactic centre. Based on more recent data releases, these enriched stars have been identified out to large distances up to ∼ 15 kpc by Horta et al. (2021b). The large population of N-rich stars identified by Schiavon et al. (2017a) is suggested to contribute a minimum of 19-25% to the stellar mass in the inner ∼2 kpc of the halo[1]. Looking at the halo stars with $|z| > 10$ kpc, Martell et al. (2016) find the contribution to the stellar mass budget due to GC dissolution to be ∼ 2%. Such a large spatial variation of the frequency of N-rich stars has been quantified by Horta et al. (2021b). By taking into account the APOGEE selection effects, they measure a ratio of $\sim 17^{+10}_{-7}\%$ and $\sim 3^{+1}_{-0.8}\%$ at $R_{GC} \sim 1.5$ kpc and $R_{GC} \sim 15$ kpc, respectively.

With the availability of *Gaia's* high-quality parallaxes and the resulting 6D phase-space information, orbital parameters and IOM for Milky Way stars can be estimated. Since these properties are essentially invariant in low-density regions of the Milky Way, they can be used to group stars according to orbital properties that are associated with those of the progenitor system. Recent studies concerning the origins of enriched stars in the halo which show similar abundances to those of SG GCs have investigated the likelihood that these enriched stars originate from GCs (Carollo et al., 2013; Savino & Posti, 2019;

---

[1] To obtain these numbers, Schiavon et al. (2017a) applied the Besançon models (Robin et al., 2012, 2014) in order to estimate the contribution of the inner stellar halo to the mass budget of the inner Galaxy.

Tang et al., 2020; Hanke et al., 2020). Savino & Posti (2019) directly compare the IOM of 57 CN-strong field stars, observed in SEGUE (Yanny et al., 2009) and SEGUE-2 (Eisenstein et al., 2011) surveys, to those of known Milky Way globular clusters. They find that ∼70% of their sample of field stars have halo-like orbital properties, with only 20 stars having a likely orbital association with an existing globular cluster. They do, however, claim that the orbital properties of halo stars seem to be compatible with the globular cluster escapee scenario. Similarly, Tang et al. (2020) compare the kinematics of ∼100 N-rich stars in LAMOST DR5 (Zhao et al., 2012) to N-normal metal-poor field stars. They conclude that the orbital parameters of N-rich field stars indicate that most of them are inner-halo stars and that the kinematics of these stars support a possible GC origin. Note that Bekki (2019) propose an alternative scenario where N-rich stars are produced in the high-density building blocks of the bulge rather than GCs.

In this chapter, we aim to constrain the origin of N-rich stars located in the Galactic bulge, on the basis of their chemo-dynamical properties. Identifying a population of accreted and *in situ* N-rich stars defined chemically, which are also confirmed by kinematics, we find that the ratio of N-rich to N-normal differ substantially between accreted and *in situ* populations.

This chapter is organised as follows: In Section 2.2 we describe the data and the criteria for our sample. The results are presented and discussed in Section 2.3, and our conclusions are summarised in Section 2.4.

2.2 Data & Sample

The results in this chapter are based on elemental abundances, radial velocities and stellar parameters from Data Release 16 of the APOGEE-2 survey (Majewski et al., 2017; Blanton et al., 2017; Ahumada et al., 2020) and proper motions from *Gaia*-DR2 (Gaia Collaboration et al., 2016, 2018). We make use of the publicly available code `galpy`[2] (Bovy, 2015; Mackereth & Bovy, 2018) to calculate orbital parameters adopting a McMillan (2017) potential. We also use distances from Leung & Bovy (2019b) which are generated using the astroNN python package (Leung & Bovy, 2019a). The distances are determined using a training set that comprises APOGEE spectra and *Gaia*-DR2 parallax measurements for the purpose of predicting stellar luminosity from spectra. The model is able to simultaneously predict distances and accounts for the parallax offset present in *Gaia*-DR2, producing high precision, accurate distance estimates for APOGEE stars, which match well with external catalogues and standard candles.

---

[2] `http://github.com/jobovy/galpy`

2.2.1 APOGEE DR16

APOGEE-2, one of the four SDSS-IV (Blanton et al., 2017; Ahumada et al., 2020) experiments, has obtained near-infrared (NIR), high SNR (S/N $>$ 100 pixel^{-1}) and high resolution (R $\sim 22,500$) H-band spectra for more than 450,000 Milky Way stars, from which precision radial velocities, stellar parameters, and abundances for up to 26 elements are determined. APOGEE-2 uses two twin NIR spectrographs (Wilson et al., 2019) attached to the 2.5 m telescopes at Apache Point (Gunn et al., 2006), and Las Campanas Observatories (Bowen & Vaughan, 1973). A more in-depth description of the APOGEE survey, target selection, raw data, data reduction and spectral analysis pipelines can be found in Majewski et al. (2017), Zasowski et al. (2017), Holtzman et al. (2015), Jönsson et al. (2018), Nidever et al. (2015), respectively (see Jönsson et al. (2020) for a complete up-to-date description of the latest APOGEE data released in DR16). The data are first reduced (Nidever et al., 2015 & Jönsson et al., 2020) using the APREAD and APSTAR pipelines, respectively. The data are then fed into the APOGEE Stellar Parameters and Chemical Abundance Pipeline (ASPCAP; García Pérez et al., 2016; Jönsson et al., 2020), which uses libraries of synthetic spectra (Zamora et al., 2015; Holtzman et al., 2018; and Jönsson et al., 2020) calculated using customised H-band line list (Shetrone et al., 2015; Smith et al., 2021), from which outputs are analysed, calibrated and tabulated (Holtzman et al., 2018; Jönsson et al., 2020).

2.2.2 Sample selection

We restrict our sample to stars that have `ASPCAPFLAG` $= 0$, SNR > 70 and distance uncertainty $< 20\%$ (i.e. d_{err}/d < 0.2). By performing these cuts, we obtain a reduced sample of APOGEE DR16 for which we can obtain reliable chemo-dynamic information. A further cut of $\log g < 3$ is also made to remove dwarf stars.

In addition, to ensure our sample is free from any stars residing in existing GCs, we remove from our sample any stars belonging to the GC member list from Horta et al. (2020). Furthermore, this chapter focuses on stars in the Galactic bulge, so we make a spatial cut and select only stars with Galactocentric distance $R_{GC} < 4$ kpc. The effective temperature of these stars is further constrained to the range 3250 K $< T_{\rm eff} <$ 4500 K. The lower $T_{\rm eff}$ limit is adopted to avoid very cool stars whose elemental abundances are affected by important systematic effects, where spectral lines at low temperatures are unclear and make it difficult for the pipeline to distinguish. The upper limit aims to eliminate from the sample C and N abundances that are uncertain due to the weakness of CN and CO lines in spectra of warm stars with relatively low metallicity ([Fe/H] < -1). The bulge selection criteria can be summarised as:

1. `ASPCAPFLAG` $= 0$
2. $R_{GC} < 4$ kpc
3. $d_{err}/d < 0.2$
4. $3250 \text{ K} < T_{\text{eff}} < 4500 \text{ K}$
5. $\log g < 3$
6. SNR > 70

To select our sample of N-rich stars, we follow the sigma clipping methodology implemented in Schiavon et al. (2017a). By inspecting the bulge stars in the [N/Fe]-[Fe/H] plane, N-rich stars are defined as those deviating by more than 5.5σ from a 4th-order polynomial fit to the data in the bulge sample (see Figure 2.1). The polynomial is given by:

$$\begin{aligned} [\text{N/Fe}] = \; & 0.256 + 0.239\,[\text{Fe/H}] - 0.072\,[\text{Fe/H}]^2 \\ & - 0.304\,[\text{Fe/H}]^3 - 0.091\,[\text{Fe/H}]^4 \end{aligned} \tag{2.1}$$

We further restrict these N-rich stars to those with [C/Fe] < 0.15, in order to limit our sample to stars which present the typical N-C anti-correlation of SG GC stars. Application of these selection criteria leaves us with a sample of 83 N-rich stars within the bulge sample of 14,448 stars.

In this chapter, we adopt a more stringent threshold of 5.5 σ to define N-rich stars than the 4 σ threshold adopted by Schiavon et al. (2017a). In both cases, the threshold decision was informed by the distribution of the selected N-rich stars in the [N/Fe]–[C/Fe] abundance plane, where N-rich stars display an anticorrelation between those two abundance ratios. The threshold was chosen so as to clean the N-rich sample from contaminants due to abundance errors and statistical fluctuations. That philosophy is aimed at prioritising N-rich sample purity over completeness. That our threshold is more stringent than that adopted by Schiavon et al. (2017a) reflects the fact that our parent sample is considerably larger, requiring a larger threshold to minimise contamination by outliers due to statistical fluctuations.

We also look at the possible contamination to our sample of N-rich stars by AGB stars, which can also present an abundance pattern characterised by Nitrogen enrichment and Carbon depletion (Renzini & Voli, 1981b; Charbonnel & Lagarde, 2010; Ventura et al., 2013). We identified 5 N-rich AGB candidates by their position on the $\log g - T_{\text{eff}}$ plane, hand-picking those that have low $\log g$, high T_{eff} and relatively high [Fe/H] compared to other stars in their neighbourhood, corresponding to ~6% of the sample, in agreement

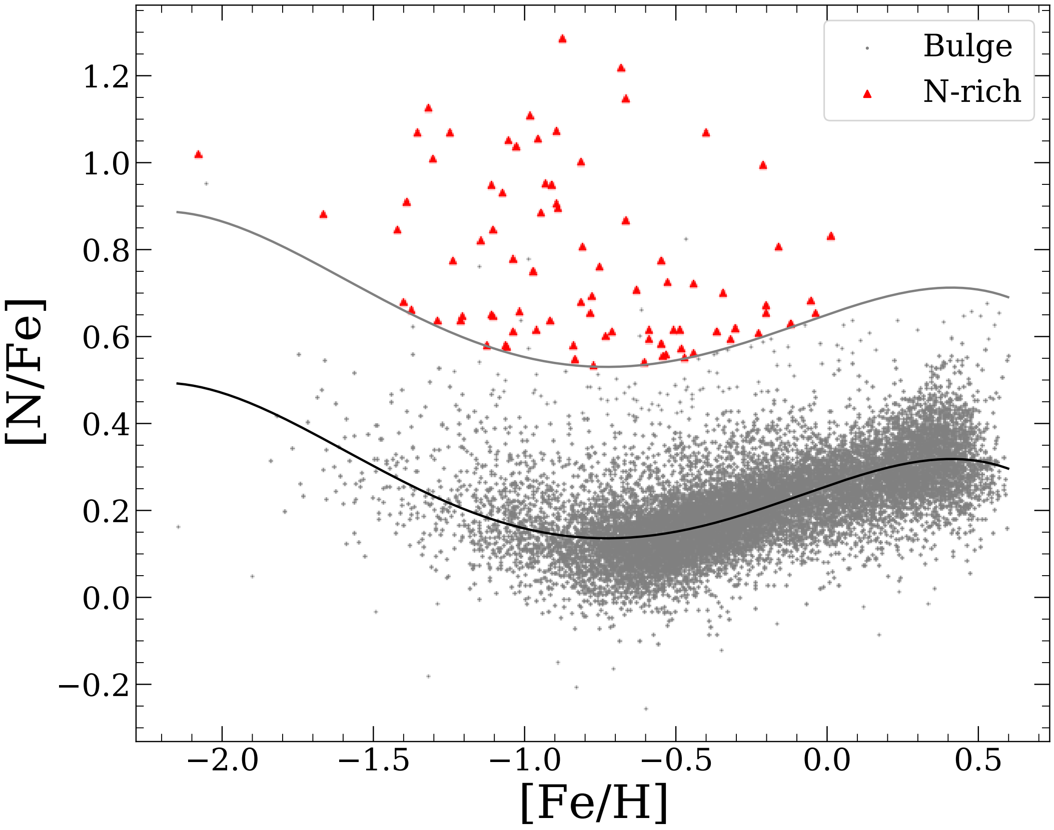

FIGURE 2.1: Distribution of sample stars in [N/Fe]-[Fe/H] plane. The small grey dots show the bulge population as selected in Section 2.2.2. The red triangles indicate the N-rich stars, defined as stars which deviate from the 4^{th} order polynomial fit (black line) by more than 5.5σ and have [C/Fe] < 0.15.

with theoretical expectations (Girardi et al., 2010). Due to the difficulty of individually selecting AGBs in our large sample of bulge field stars, we decide to keep the N-rich AGBs in our sample for consistency. We note that the results of this chapter are largely unaffected by the presence of these N-rich AGBs.

2.3 Results

In this section, we discuss how our sample of accreted and *in situ* populations are selected, employing methods used in Mackereth et al. (2019). We then discuss how these populations differ from each other in orbital space, and show the similarities of the N-rich stars to GC members in chemical space.

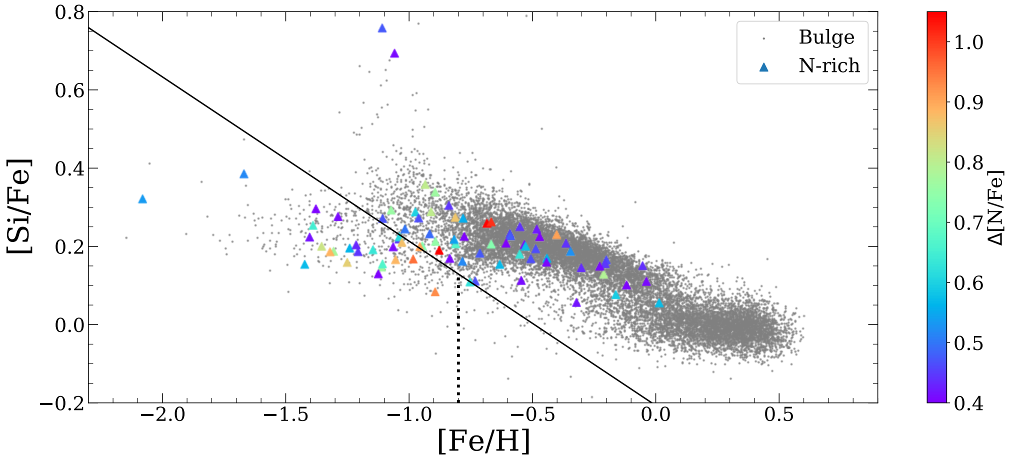

FIGURE 2.2: Distribution of sample stars in [Si/Fe]-[Fe/H] plane. The grey points show the distribution of the bulge stars, and the triangles, coloured according to the [N/Fe] residuals of the polynomial fit shown in Figure 2.1, show the N-rich stars distribution in this plane. The solid black line is the cut made to separate the accreted stars from the *in situ* stars shown in Mackereth et al. (2019), adjusted to account for the metallicity gradient of disc populations between the outer and inner halo. The cut of [Fe/H] < -0.8 to remove disc contaminants is shown as the vertical dotted line.

2.3.1 Selecting accreted and *in situ* stars

In order to split our sample into accreted and *in situ* groups, we study the distribution of stars in the α-Fe plane. Mackereth et al. (2019) achieved that by examining the distribution of their sample in the Mg-Fe plane, whereas Horta et al. (2021a) focused on the distribution in the [Mg/Mn] vs [Al/Fe] plane. We cannot proceed in the same way, because the abundances of Al and Mg are affected by the multiple populations phenomenon in GCs (e.g., Bastian & Lardo, 2018; Mészáros et al., 2015, 2020), so that the positions of N-rich stars in chemical planes involving those elements cannot be interpreted in the same way as those of normal stars. Therefore, we use Si as the tracer of α-element abundances, because this element does not present substantial star-to-star variations in Galactic GCs.

The data in Figure 2.2 show that the N-rich star population occupies the same locus in the Si-Fe plane as the overall bulge field population. Following Mackereth et al. (2019), we split the sample between accreted and *in situ* populations. To determine where the dividing line is drawn in the [Si/Fe] vs [Fe/H] plane, we proceed as follows: 1) Following Mackereth et al. (2019), we choose a slope that approximately matches the mean slope of the high- and low-α populations, slightly adjusting it to minimise the contamination of the accreted populations by low-α disc stars; 2) We calculate the distance in [Fe/H] between the dividing line and the mean value of the low-Mg disc population and adjust the zero-point so that the distance is the same in the [Si/Fe] vs [Fe/H] plane; 3) We further shift the zero-point by +0.2 dex in [Fe/H], to account for the disc metallicity gradient (e.g., Hayden et al., 2015). The resulting linear relation is given by:

$$[\mathrm{Si/Fe}] = -0.42\,([\mathrm{Fe/H}] + 0.016\,) + 0.2 \tag{2.2}$$

Because this relation may be considered somewhat arbitrary, we estimate how a ±0.1 dex zero-point variation impacts our results (see discussion in Section 2.3.3)

We make a further cut in metallicity to the accreted population of $[\mathrm{Fe/H}] < -0.8$, to minimise contamination from disc stars. This latter cut removes 38 bulge stars from our accreted population, bringing the total number of bulge stars down to 14,410. We henceforth refer to stars below (above) and to the left (right) of the dividing line as "accreted" (*in situ*) populations. The resulting accreted and *in situ* general bulge samples comprise 428 and 13,982 stars, respectively, with 25 N-rich stars being located in the accreted locus, and 58 located in the *in situ* region. Thus, we conclude that roughly ∼30% of the N-rich stars in the inner Galaxy have an accreted origin. We emphasise here that stars in each sub-sample are found across the entire inner Galaxy.

Figure 2.3 shows where these sub-samples lie in the [Al/Fe]-[N/Fe] plane. By placing stars in this plane, former GC members can be identified as those that follow a positive correlation between those two abundance ratios. When displaying our sample on this plane, we can see that the accreted and *in situ* bulge populations occupy slightly different loci. While N and Al abundances of N-rich stars are correlated in both *in situ* and accreted sub-samples, the correlations in each sub-sample are slightly different. The [Al/Fe] ratios of N-normal stars in the accreted sample, save for a handful of outliers, are lower than those in their *in situ* counterparts, on average by ∼ 0.2 dex. This result validates our definition of accreted vs *in situ* populations, since the accreted stars with first-generation-like abundance patterns (i.e., those not affected by multiple population effects) are consistent with a dwarf galaxy origin (e.g., Mackereth et al., 2019; Helmi, 2020; Das et al., 2020; Horta et al., 2021a).

We identify a group of Si-rich stars, with $[\mathrm{Si/Fe}] \geq +0.5$ in the metallicity range $-1.3<[\mathrm{Fe/H}]<-0.9$. They are similar to those spotted by Masseron et al. (2019) within the MW GCs M92, M15 and M13. Those authors showed that, in the most metal-poor GCs, M92 and M15, Si-rich stars are characterised by very low [Mg/Fe], whereas stars in M13 had normal [Mg/Fe]. The Si-rich stars in our sample have normal [Mg/Fe], resembling those of Masseron et al. (2019) identified in M13. The origin of these Si-rich stars is unclear. While their presence in the GCs studied by Masseron et al. (2019) suggests a GC dissolution origin, Masseron et al. (2020a) identified Phosphorus-rich stars with inner halo orbits, which also present elevated [Si/Fe]. The nucleosynthetic origin of these P-rich stars is not explained, although Masseron et al. (2020a) discusses several

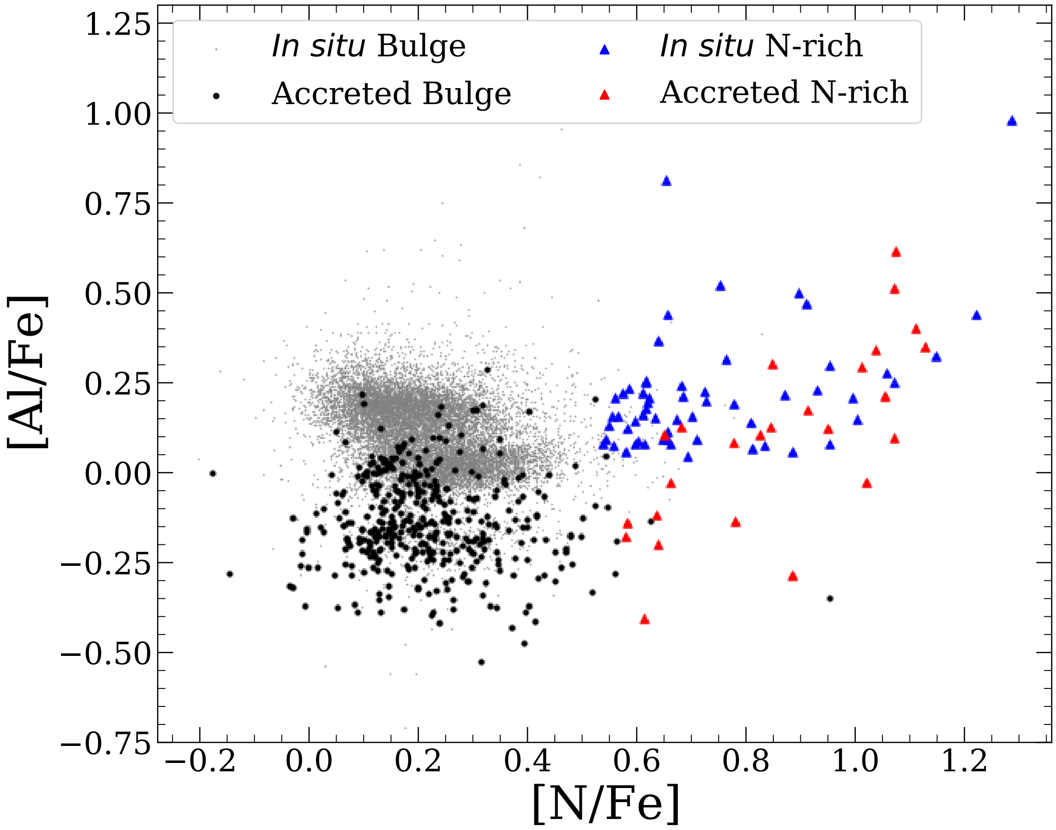

FIGURE 2.3: Distribution of *in situ* bulge (small grey dots), accreted bulge (black dots), *in situ* N-rich (blue triangles) and accreted N-rich (red triangles) stars in [Al/Fe]-[N/Fe] plane. The N-rich stars show a correlation between [N/Fe] and [Al/Fe], which is also observed in SG GC stars. However, the correlations are slightly different between the accreted and *in situ* populations. The accreted bulge stars are seen to occupy a lower locus in [Al/Fe] than the *in situ* by ~ 0.2 dex, which is consistent with a dwarf galaxy origin.

alternatives. The detailed abundance patterns of these stars, presented by Masseron et al. (2020b) show enhancements in C, O, Mg, Si and Al. Our Si-rich stars show mild-to-strong enhancements in these elements, though they present normal [P/Fe]. If one assumes that the latter is due to uncertainties in the APOGEE P abundances, our Si-rich stars could conceivably be associated with the P-rich phenomenon. Further scrutiny in the form of additional abundance studies is advised. For the purposes of this study, we ascribe a GC origin to these field Si-rich stars and discuss their kinematic properties in Section 2.3.3. Our conclusions are not affected by this assumption.

2.3.2 Comparison with GCs

To confirm the association of the field N-rich stars with GCs, we over-plot our sample of N-rich stars on data for GC members from Horta et al. (2020) in three different

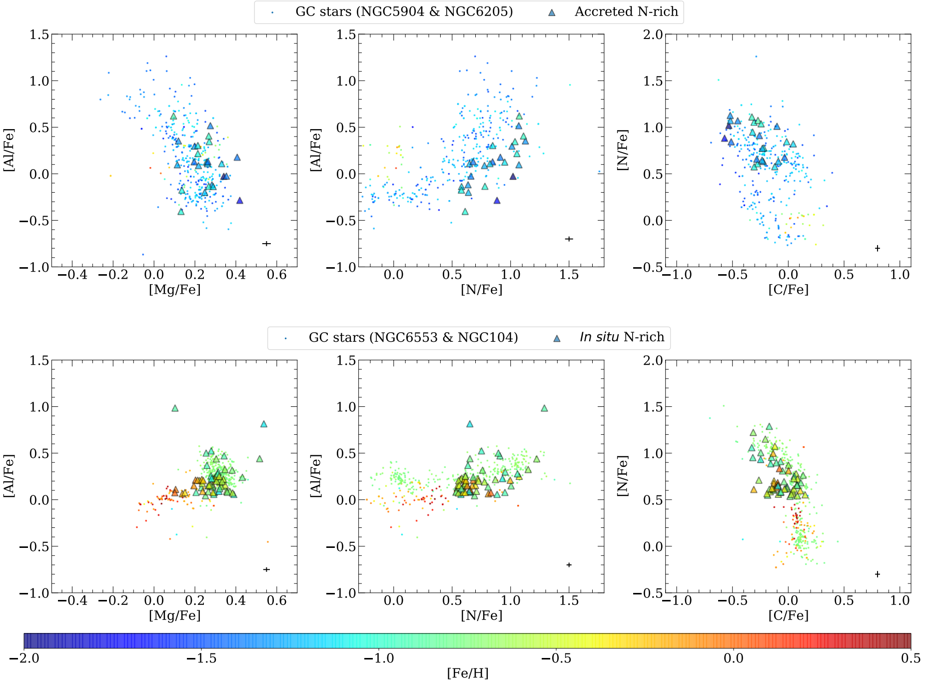

FIGURE 2.4: Coloured dots and triangles indicate GC stars (Horta et al., 2020) and N-rich stars (see Section 2.2.2), respectively, colour coded by their [Fe/H] abundance. The graphs on the top row show the accreted N-rich stars plotted on top of stars in NGC5904 and NGC6205, and the bottom graphs show the *in situ* N-rich stars plotted on top of stars in NGC6553 and NGC104, both using the same metallicity colour scale. Each plot shows the mean error bar for the N-rich stars in the bottom right corner. The 1^{st} column shows these stars in the [Al/Fe]-[Mg/Fe] plane to show the Al-Mg anti-correlation in GCs. The 2^{nd} column shows the distribution in the [Al/Fe]-[N/Fe] plane to show the Al-N correlation in GCs. The 3^{rd} column shows the distribution in the [N/Fe]-[C/Fe] plane to show the N-C anti-correlation in GCs. Each plot shows that our sample of N-rich stars lies on the same locus as SG GC members, supporting the idea they have possible GC origin.

chemical planes. We show the correlations of GC stars in Mg-Al, Al-N and N-C space. In each panel, the N-rich stars lie on the same locus as SG GC stars, which supports our assumption that they are, in fact, former GC members. For clarity, the accreted and *in situ* populations are plotted on different panels of Figure 2.4 because they span different metallicity regimes. Abundances of field stars in each set of panels are compared with those of members of GCs whose mean chemical compositions locate them in the accreted and *in situ* loci of the Si-Fe plane. For the comparison with accreted N-rich stars we select NGC5904 (258 stars, <[Fe/H]> = -1.14, <[Si/Fe]> = 0.18) and NGC6205 (119 stars, <[Fe/H]> = -1.44, <[Si/Fe]> = 0.19), and for the *in situ* N-rich stars we select NGC6553 (52 stars, <[Fe/H]> = -0.04, <[Si/Fe]> = 0.06) and NGC104 (333 stars, <[Fe/H]> = -0.67, <[Si/Fe]> = 0.21)

On the plots in the first column, the anti-correlation between Al and Mg appears to differ substantially between the metal-poor and metal-rich sub-samples of GCs. The metal-rich GC sub-sample shows a smaller range in both [Al/Fe] and [Mg/Fe] than those shown by the metal-poor sub-sample. Therefore, while the anti-correlation is easily visible in the metal-poor sample, it is not evident in the metal-rich sample. This is similarly shown in the Al-N plots. Where although the correlation can be seen in the metal-rich GCs, it is more easily identified in the metal-poor GC sub-sample. For a more detailed discussion, see Mészáros et al. (2015) and Nataf et al. (2019).

In a recent paper, Fernández-Trincado et al. (2019) claim that N-rich stars must have [Al/Fe] $>$ +0.5 to be considered SG GC members. Application of that criterion would remove large numbers of N-rich stars from our sample. However, we argue that our sample of field N-rich stars are indeed akin to SG GC members for the following reason: the rightmost panels of Figure 2.4 show a clear bimodality in the [N/Fe]-[C/Fe] plane, with the SG GC stars located and higher [N/Fe] above their FG GC counterparts. The dividing line between the two populations is located roughly at [N/Fe] = +0.5 for [C/Fe] = –0.5, and gently decreasing [N/Fe] for increasing [C/Fe]. This bimodality is also present in both [Al/Fe]-[Mg/Fe] and [Al/Fe]-[N/Fe], showing that there are SG GC stars with [Al/Fe]$<$ 0.5 all the way to below solar. In fact, the application of an [Al/Fe] $>$ +0.5 cut would remove a large fraction of the SG stars in GCs themselves, particularly in the low metallicity regime (top panels of Figure 2.4). It is also well known that, although SG GCs typically present enhancements in N, Al and Na (Bastian & Lardo, 2018), not all stars in GCs that are enhanced in N are also enhanced in Al. Indeed, as mentioned above, the Al-Mg anti-correlation is dependent on metallicity, being substantially weaker in metal-rich GCs (e.g., Mészáros et al., 2015; Nataf et al., 2019; Mészáros et al., 2020), and mass (Massari et al., 2017).

2.3.3 Kinematic properties

In this sub-section, we check whether our definition of accreted and *in situ* stars, which is based solely on chemistry, maps into distinct properties in kinematic space. To do this, we make comparisons between the distributions of our samples in a kinematic diagram, which is used to distinguish components of the Galaxy on the basis of their kinematic signatures (e.g., Venn et al., 2004; Bonaca et al., 2017; Helmi et al., 2018; Koppelman et al., 2019). The x-axis of the kinematic diagram is the tangential velocity, v_ϕ, while the y-axis is the quadrature sum of the radial and vertical velocities, $\sqrt{{v_R}^2 + {v_Z}^2}$.

The accreted and *in situ* populations are displayed on the kinematic diagram separately on the left and right panels of Figure 2.5, respectively. Since the velocities are in Galactocentric coordinates, this places the origin of the coordinate system at the Galactic

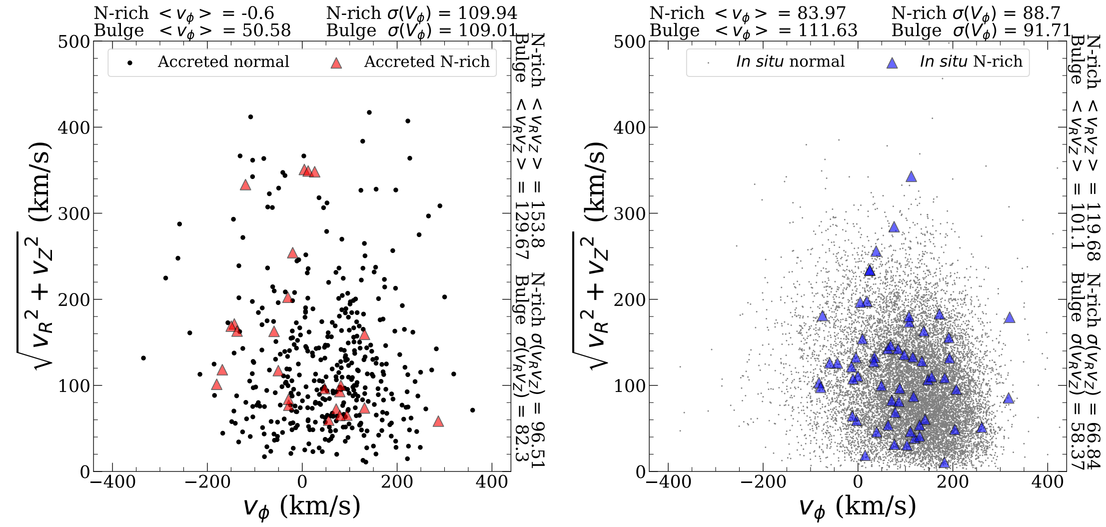

FIGURE 2.5: Distribution in $\sqrt{v_R{}^2 + v_Z{}^2}$ vs. v_ϕ of accreted and *in situ* stars on the left and right panel, respectively. *Left Panel:* Accreted N-rich stars (red triangles) and the accreted bulge stars (black dots). *Right Panel: in situ* N-rich stars (blue triangles) and *in situ* bulge stars (grey dots). Anything with $v_\phi > 0$ has a prograde orbit, similar to that of the disc, and anything with $v_\phi < 0$ has a retrograde orbit. We also show on these plots the mean and standard deviation of the sub-samples for each axis.

Centre, therefore the velocity of the Sun is at $\text{v}_{LSR} \sim 220$ km/s. In both panels, normal stars are displayed as black/gray dots and N-rich stars as coloured triangles. Visual examination of these plots suggests the following interesting trend: Accreted stars, both normal and N-rich, have on average more retrograde orbits ($\text{v}_\phi < 0$) than their *in situ* counterparts, whose orbits are predominantly prograde. This is clearly shown by the difference in the v_ϕ distribution of the *in situ* and accreted samples of N-rich stars, with the mean of the latter being ~ 80 km/s lower than that of the former.

The above visual impressions must be confirmed by a quantitative statistical evaluation. The Kolmogorov-Smirnov (KS) statistic is a nonparametric test used to assess the similarity between two samples. We use the python package `ndtest`[3] to make 2D comparisons between the distributions in v_ϕ and $\sqrt{v_R{}^2 + v_Z{}^2}$ of the following sub-samples, as shown in Table 2.1: accreted N-rich vs. accreted normal, *in situ* N-rich vs. *in situ* normal, accreted N-rich vs. *in situ* N-rich and, accreted normal vs. *in situ* normal. The KS tests result in a rejection of the null hypothesis, with p-value < 0.1 for all four comparisons. The clear kinematic distinction between the accreted and *in situ* populations confirms our chemical selection of these groups. We also note the difference between accreted N-rich vs. accreted normal sub-samples. This result can be understood by examination of Figure 2.6. In that plot, it can be seen that the accreted normal stars show a clump of slightly prograde stars around $E/10^5 \sim -2.2$ km^{2}s^{-2}, without a clear

---

[3] `https://github.com/syrte/ndtest`

Comparison	**Full Sample**	**[Fe/H]< -0.8**	**Zero-point+0.1 dex**	**Zero-point -0.1**
Accreted N-rich vs. Accreted normal	0.024	0.024	0.066	0.172
In situ N-rich vs. *In situ* normal	0.028	0.294	0.062	0.006
Accreted normal vs. *In situ* normal	< 0.001	0.038	< 0.001	< 0.001
Accreted N-rich vs. *In situ* N-rich	0.009	0.027	0.040	0.223

TABLE 2.1: p-values obtained from performing a 2DKS test between the different sub-samples shown in Fig.2.5. First Column: Results for the comparisons between sub-samples as defined in Section 2.3.1. Second Column: Result for the comparisons between the sub-samples with [Fe/H] < -0.8. Third and Fourth Column: Result when shifting the zero-point of the dividing line, equation (2), by ±0.1 dex. Setting a threshold for the p-value of 0.1. So, a p-value < 0.1 results in a rejection of the null hypothesis, whereas a p-value > 0.1 means the null hypothesis cannot be rejected.

counterpart in the N-rich accreted group. We suspect that this prograde population is likely due to contamination from the disc. In addition, the accreted normal population hosts a number of stars forming a cloud with $E/10^5 \gtrsim -1.85$ km^{2}s^{-2}, where no N-rich stars can be found. That is the locus occupied by stars belonging to the GE/S system, as well as other possible accretion events (Ibata et al., 1994; Helmi et al., 1999; Ibata et al., 2016; Belokurov et al., 2018; Haywood et al., 2018; Helmi et al., 2018; Mackereth et al., 2019; Horta et al., 2021a). Conversely, most of the N-rich stars occupy the same locus as Heracles identified recently by Horta et al. (2021a), with a couple of stars displaying kinematics suggestive of disc-like orbits.

Interestingly, the KS test rejects the null hypothesis for the similarity between the *in situ* N-rich vs. *in situ* normal sub-samples. We suggest that the difference between these two sub-samples is due to the presence of disc stars within 4 kpc of the Galactic centre. This is further discussed in Section 2.3.4

The stars in the accreted sample have on average lower metallicities than their *in situ* counterparts. Thus, the differences encountered could be due to the dependence of kinematics on the metallicity of stellar populations. To test that hypothesis, we redo the KS tests to assess the similarity between the accreted and in situ sub-samples, this time limiting the comparison to stars with [Fe/H] < -0.8. The results from this comparison are shown in Table 2.1. The difference between the N-rich and normal accreted populations remains unchanged since they were already restricted to [Fe/H] < -0.8. We do, however, see a big change in the comparison between the *in situ* populations, where the p-value $= 0.294$ tells us that the null hypothesis cannot be rejected. This is due to the removal of high metallicity disc stars from our sample of *in situ* normal stars. Regarding the comparison between accreted and *in situ* populations, for both the N-rich and normal samples, the null hypothesis is rejected even when the comparison is limited to metal-poor sub-samples. In short, accreted and *in situ* samples are kinematically different populations even when only metal-poor stars are considered.

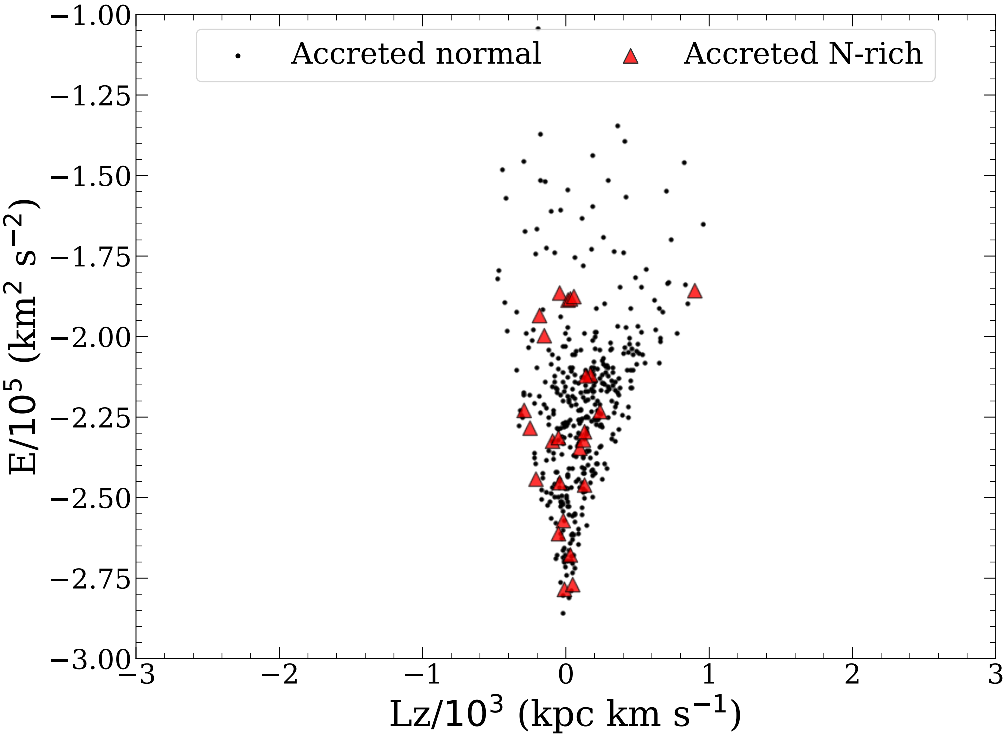

Figure 2.6: Accreted N-normal (black dots) shows a population of stars in the same locus as GE/S stars at high energies, whilst the accreted N-rich stars (red triangles) occupy the low energy region similar to Heracles. These quantities are calculated assuming an axisymmetric potential for the MW.

We checked whether our results are sensitive to the definition of the line separating accreted and *in situ* populations in Figure 2.2. For that purpose, we shifted the zero-point of the relation given by the Equation 2.2 by ±0.1 dex in [Fe/H], the results for which are shown in the fourth and fifth columns of Table 2.1. When increasing the zero-point by +0.1 dex, our results are unchanged. However, when shifting the relation towards lower [Fe/H], the KS tests become consistent with the null hypothesis for two of the sub-sample comparisons: *(i)* accreted normal vs. accreted N-rich stars. This result is due to the removal of a small number of retrograde N-rich stars and the reduction in the contribution of prograde normal stars (which we conjectured in Section 2.3.3 to be due to disc contamination); *(ii)* accreted N-rich vs. *in situ* N-rich stars. This happens because the above-mentioned retrograde N-rich stars that are moved from the accreted to the *in situ* sub-sample, make the two groups more similar kinematically. Since this exercise leads to a reduction of the size of the N-rich accreted population, we deem these results of little statistical significance. The matter will have to be revisited on the basis of larger samples.

Again, we check the dependence of kinematics on metallicity by limiting the comparison to stars with [Fe/H] < -0.8, as done above, after shifting the relation by ± 0.1 dex. The results for this are not shown since the only change we find is when comparing *in situ* N-rich and *in situ* normal sub-samples. In both cases, when moving the zero-point towards higher or lower [Fe/H], the null hypothesis cannot be rejected when comparing these two sub-samples. Also in this case the statistical significance of the results is small due to the reduced sample sizes.

Finally, we examine the kinematic properties of Si-rich stars mentioned in Section 2.3.1, separately. When comparing their properties to those of N-rich and N-normal, the KS tests only yielded a statistically significant difference with the accreted N-rich, p-value=0.022. This suggests that this population is likely to result from the dissolution of *in situ* GCs and in the remainder of this analysis they will be treated as such.

In summary, the results above show that the chemistry-based definition of accreted and *in situ* sub-samples maps into distinct kinematic properties. Both N-rich and N-normal *in situ* samples with $R_{\rm GC} < 4$ kpc show more disc-like orbits than their accreted counterparts, according to expectations. In Horta et al. (2021a) we showed that there is important contamination of the chemically defined accreted samples by *in situ* stars. However, the differences persist even when controlling for the dependence of kinematics on metallicity, which argues in favour of our interpretation of the origin of the accreted N-rich sample.

2.3.4 N-rich stars frequency in accreted and *in situ* samples

An important clue to the origin of N-rich stars is their frequency, f_{Nr}, defined as the ratio between the number of such stars and the total field population (e.g., Martell et al., 2016; Schiavon et al., 2017a; Koch et al., 2019; Horta et al., 2021b). We measured this frequency in both the accreted and *in situ* sub-samples, and henceforth express it in terms of percentages. In the accreted group we find $f_{Nr} = 5.84 \pm 1.28\%$, whereas, for the *in situ* group, the measured frequency is an order of magnitude lower, $f_{Nr} = 0.41 \pm 0.05\%$, $f_{Nr} = 0.60 \pm 0.08\%$ if only high-α stars are considered. If we account for the Si-rich stars identified in Section 2.3.1, ascribing them to an *in situ* GC origin based on their kinematics, the frequency of the *in situ* group increases to $f_{Nr} = 0.58 \pm 0.06\%$, $f_{Nr} = 0.86 \pm 0.10\%$ if only high-α stars are considered. Thus, consideration of Si-rich stars does not alter our finding of a large difference between accreted and *in situ* N-rich stars.

This difference cannot be easily understood. According to the prevailing scenario for GC formation and destruction, (Kruijssen, 2014, 2015; Pfeffer et al., 2019) Galactic GCs originate from two different channels. The *ex situ*, or accreted, channel would

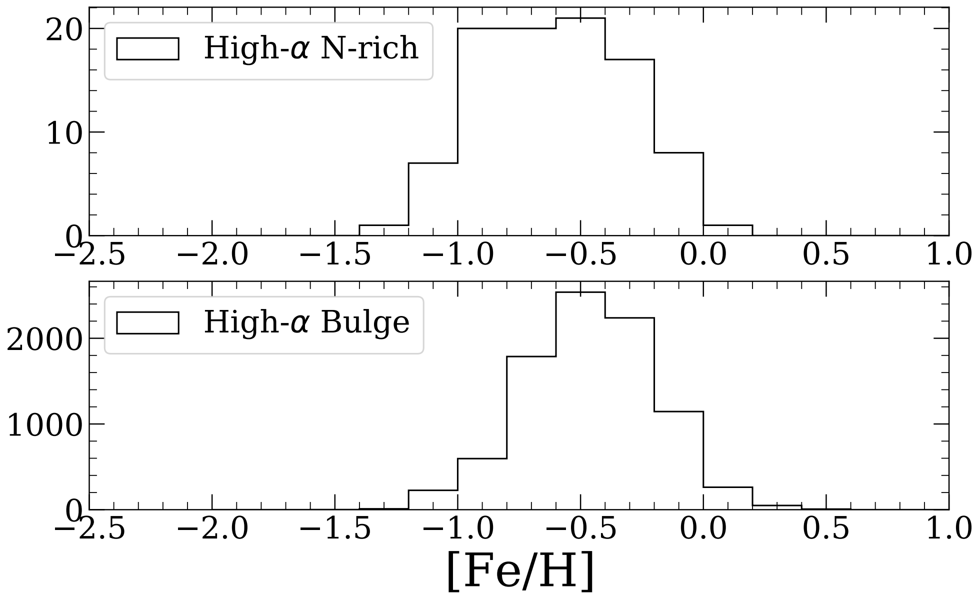

FIGURE 2.7: Metallicity distribution functions (MDFs) for the *in situ* high-α N-rich stars (top panel) and *in situ* high-α normal field (bottom panel). The MDFs of the two populations are not very different. The N-rich MDF peaks at a slightly lower [Fe/H], but is substantially broader, overlapping the high metallicity end of the N-normal MDF.

consist of GCs that were accreted to the Galaxy along with their host galaxies. Those accretion episodes occurred predominantly, though not exclusively, in the early stages of the Milky Way assembly, as suggested by various lines of evidence (e.g., Deason et al., 2014; Mackereth et al., 2018, 2019; Pfeffer et al., 2019; Schiavon et al., 2020; Hughes et al., 2020). Conversely, the *in situ* population would be comprised of GCs that were formed in the turbulent disc of the Milky Way at $z \sim 2-3$. According to this scenario, *in situ* GCs would have been destroyed very efficiently by tidal interaction with giant molecular clouds in the early disc (the so-called "cruel cradle effect", see Kruijssen et al., 2012), whereas destruction of accreted GCs via tidal stripping and evaporation was less efficient, having happened on a much longer timescale. Given these predictions, we would naively expect the frequency of *in situ* N-rich stars to be higher, not lower than that of the accreted population.

One possible way out of this conundrum is to invoke that the ratio between integrated star formation in the form of GCs over total was lower in the *in situ* than in the accreted population. This could be achieved, for instance, if the *in situ* population underwent a longer star formation episode than that leading up to the formation of the accreted population. If *in situ* star formation was extended further in time, after the cessation of the main episode of GC formation/destruction, a low *in situ* f_{Nr} could possibly be accommodated. In such a situation, however, one would expect the metallicity distribution function (MDF) of the *in situ* normal population to have more power towards higher metallicities than that of the *in situ* N-rich population.

This qualitative prediction does not seem to be supported by the metallicity distribution functions (MDFs) of the N-rich and N-normal bulge *in situ* samples, shown in Figure 2.7. For simplicity, we limit our comparison to high-α N-rich and normal field stars, as those are understood to have undergone a coherent chemical evolution path that is independent of the low-α disc population (Mackereth et al., 2018). In that figure, one can see that the MDFs of the high-α N-rich and N-normal *in situ* samples are not very different. The MDF of the high-α N-rich population peaks at [Fe/H]$\sim$–0.8, whereas that of the high-α N-normal population peaks at slightly higher metallicity, around [Fe/H]$\sim$–0.5. That difference in the mode of the two MDFs is slightly offset by the fact that the N-rich population has a broader MDF, with FWHM$\sim$0.9 dex, whereas that of the *in situ* population has FWHM$\sim$0.6 dex. Assuming the N-rich MDF reproduces that of the parent GCs, one would thus conclude that the star formation history associated with the N-normal population did not extend in time much further past the period of GC formation and destruction. This result is additionally corroborated by recent evidence for a very fast overall formation of both the high- and low-α stellar populations in the inner Galaxy, which is attested by their predominantly old ages (e.g., Hasselquist et al., 2020).

This result prompts interesting considerations on the origin of the accreted N-rich stars currently inhabiting the inner Galaxy. The frequency of metal-poor N-rich stars as a function of Galactocentric distance has been shown by Horta et al. (2021b) to undergo a steep decrease towards growing $R_{\rm GC}$ (see also Martell et al., 2016; Koch et al., 2019). At $R_{\rm GC} \sim 15$ kpc, Horta et al. (2021b) found $f_{Nr} \sim 3^{+1}_{-0.8}\%$, which is considerably lower than the ratio we find for the accreted population. Since the population of N-rich stars in our sample at low metallicity is dominated by accreted stars, this result leads to the conclusion that GC destruction associated with satellite mergers must have been very efficient in the early stages of the Galaxy's formation. Indeed it has been shown by Pfeffer et al. (2020) that GCs associated with the earliest accretion events ended up in strongly bound orbits, driven by dynamical friction. That is the case for Heracles (Horta et al., 2021a), a $\sim 5 \times 10^8$ $M_\odot$ satellite that likely merged with the MW over 10 Gyr ago (see also Kruijssen et al., 2020). Given the coincidence between the positions of our bulge N-rich stars in integrals of motion space and those of Heracles stars (Figure 2.6), we speculate that the bulge N-rich population is partly made of members of GCs that were originally associated with Heracles and were mostly destroyed during the accretion event. It is also possible that those accreted N-rich stars were already in the field of Heracles before they were accreted to the MW, however, there currently is no evidence for the presence of N-rich stars in the fields of dwarf satellites of the MW.

Hughes et al. (2020) used the E-MOSAICS simulations (Pfeffer et al., 2019) to calculate the contribution of destroyed GCs to field populations in the bulges of MW-like galaxies, comparing the predictions with the measurements by Schiavon et al. (2017a). They show that, for most of the MW-like galaxies in their simulated volume, the prediction for f_{Nr} of the *metal-poor* stellar population is lower than the observations by factors of ∼2–30 (bottom panel of their Figure 4). However, for a few simulated galaxies, the predicted f_{Nr} are in good agreement with the observations. Like the MW, the disc populations of those galaxies are characterised by a bimodal distribution in the α-Fe plane, which is a distinctive feature of the MW disc populations (e.g., Hayden et al., 2015; Mackereth et al., 2017). Mackereth et al. (2018) showed that this feature is associated with an atypical accretion history, characterised by intense merging in early times and relative calm since $z \sim 1-1.5$. It is noteworthy, however, that Hughes et al. (2020) predictions for these few MW-like galaxies differ from our measurements with regards to the dependence of f_{Nr} on the position in the α-Fe plane. The high frequency of ex-GC stars in the field of simulated galaxies is predominantly due to high-α *in situ* GC formation and destruction, whereas our data show that the high f_{Nr} in the MW bulge is due to the contribution by the dissolution of low-α *accreted* GCs. This discrepancy would be alleviated if some of the stars in the accreted region in Figure 2.2 were in fact formed *in situ*, (see Figure 2 of Hughes et al., 2020), but it is not clear that accounting for such contamination would completely eliminate the disagreement.

2.4 Summary

The results presented in this chapter make use of elemental abundances from APOGEE DR16 along with data from *Gaia* DR2 to study the chemical and kinematic properties of 83 N-rich stars located within the inner 4 kpc of the Galaxy. Our conclusions can be summarised as follows:

- We find that there are likely accreted and *in situ* components to the N-rich population within 4 kpc of the Galactic centre, identified via chemistry by making a cut in [α/Fe]-[Fe/H] space towards low metallicities (as shown in Figure 2.2) (e.g. Hayes et al., 2018; Mackereth et al., 2019; Das et al., 2020). By making this cut and removing stars without proper motions in *Gaia*, we select 428 and 13,982 bulge stars that lie in the accreted and *in situ* positions, respectively, with 25 N-rich stars being located in the accreted, and 58 located in the *in situ* locus.
- We show that our sample of N-rich stars occupies the same locus as so-called second-generation GC stars, supporting the idea that they are the by-products of GCs destruction/evaporation.

- We find that there is a significant difference in the kinematic properties of chemically defined accreted and *in situ* populations. This shows that our chemistry-based distinction of these populations maps into differences in kinematic space. We also find that the accreted bulge field population includes stars which share orbital properties with the GE/S system, although no N-rich stars occupy that locus of orbital parameter space. The absence of N-rich stars associated with GE/S in the bulge is likely due to their low frequency, combined with the relatively small number of GE/S stars found in the bulge (see Horta et al., 2021a)

- We find that the frequency of N-rich stars differs by an order of magnitude between the accreted ($f_{Nr} = 5.84 \pm 1.28\%$) and *in situ* ($f_{Nr} = 0.41 \pm 0.05\%$) samples. This result seems to be at odds with numerical simulations that predict a higher frequency of destroyed GCs among high-α *in situ* populations (Hughes et al., 2020). We speculate that the higher frequency of N-rich stars among accreted populations is due to early merger events, such as Heracles (Horta et al., 2021a), which likely had their GCs destroyed very efficiently during the merger with the MW.

- The identification of an accreted population of N-rich stars in the bulge raises the question of whether the GCs from which they originate were destroyed in their host dwarf galaxies or during the merger. If the former hypothesis is correct, we would expect that N-rich stars would be present in the field of current Milky Way satellites. Norris et al. (2017) did not find a Na-O anti-correlation, which is typical of GC stars, in Carina dwarf spheroidal field stars. However, their study is based on a sample of 63 stars, which is relatively small. Since the observed frequency of N-rich stars in the halo is $\sim 3\%$ one would expect to find ~ 2 N-rich stars in the sample of Norris et al. (2017). Such low numbers could easily be missed due to stochastic sampling.

Chapter 3

In-depth analysis of the Splash

3.1 Introduction

Galactic Archaeology has seen a lot of major advancements in recent years with large-scale surveys such as the Sloan Digital Sky Survey (SDSS, Blanton et al., 2017), the Apache Point Galactic Evolution Experiment (APOGEE, Majewski et al., 2017), and *Gaia* (Gaia Collaboration et al., 2018) leading up to the discovery of substructures in the Milky Way halo (Belokurov et al., 2006; Schiavon et al., 2017a; Helmi et al., 2018; Haywood et al., 2018; Belokurov et al., 2018; Mackereth et al., 2019; Naidu et al., 2020; Horta et al., 2021a). Among these discoveries was the identification of what is called the *in situ* halo, a structure within the MW with chemistry similar to the high-α disc but with halo-like kinematics (Bonaca et al., 2017; Di Matteo et al., 2019; Belokurov et al., 2020). It is proposed that this structure is the product of the heating of the MW disc (McCarthy et al., 2012; Cooper et al., 2015). By combining data from a variety of sources Belokurov et al. (2020) took to study the chemodynamic properties of the thin and thick disc and the halo of the solar neighbourhood. They identify the *in situ* halo as a large population of metal-rich stars ([Fe/H] > -0.7), which they dub the 'Splash'. This stellar population overlaps with the thick disc in multiple properties, in particular their chemical compositions, as measured by the ratio between the abundances of α-elements and Fe ([α/Fe]), and the velocity dispersion. Therefore, they hypothesise that the origin of the Splash is linked to the old thick disc.

While the properties of Splash stars are similar to those of their thick disc counterparts, their orbits are far more eccentric (Mackereth et al., 2019; Belokurov et al., 2020). Moreover, Splash stars are found to be older than thick disc stars, yet slightly younger than the majority of the known accreted structures (e.g. GE/S, Helmi et al., 2018; Belokurov et al., 2018). Belokurov et al. (2020) show that the age distribution of the Splash is truncated around the ages of the youngest stars associated with GE/S. Similarly, on the basis of *Gaia* data, Gallart et al. (2019) show that the *in situ* disc of the MW has a second peak of star formation, which they use to date the merger event at around 9.5 Gyr. On the other hand, based on ages for a sample of sub-giants from the LAMOST survey (Cui et al., 2012), Xiang & Rix (2022) show a single peak age distribution of the thick disc population, and dated the merger event to coincide with the peak of star formation at 11.2 Gyr ago, just after the youngest stars in the Splash and just when the merger with GE/S was completed.

These findings lead to the suggestion that the merger of GE/S caused the heating of the disc which resulted in the Splash. Such an interpretation of the data makes the Splash a very interesting population as it may contain the oldest stellar population in the MW disc, so its study should provide crucial information about the early stages of Galactic disc formation. Further studies of the MW disc by Belokurov & Kravtsov (2022) reveal a more metal-poor population of *in situ* stars, with kinematics and chemistry that differ from those of the Splash. The chemical composition of this more metal-poor population, which they name Aurora, differs clearly from that of the Splash at [Fe/H]=–0.9, showing a larger scatter in many abundances. Aurora also has a larger scatter in its tangential velocity distribution, than what is seen in the Splash, cementing it as a different population.

Along with large-scale surveys we have also seen improvements in numerical simulations to the point where high-resolution MW-like zoom-ins are a good match to detailed properties of the Milky Way. This provides us with a much larger sample of galaxies which can be used to see where the MW fits in comparison, while also guiding the interpretations of observational data. Two recent simulation-based works that study the effects of mergers on the heating of the disc are Grand et al. (2020) and Dillamore et al. (2022), which make use of simulations from the `AURIGA` project (Grand et al., 2017, 2018) and `ARTEMIS` (Font et al., 2020), respectively. Both papers reveal similar results with respect to the age of the Splash and the relation between the Splash fraction and the Most Massive Accreted Progenitor (MMAP) mass. They find the age of the youngest Splash stars to coincide with the end of the GE/S-like merger, in line with the results from Belokurov et al. (2020). Grand et al. (2020) propose that right after the end of the merger event there is a burst of star formation in the host galaxy. This starburst population and its properties are something to look out for in observational data. Similarly, Dillamore et al. (2022) show a similar starburst after the end of the MMAP accretion in most of their galaxies. They also examine what happens to the Splash population, which they define as *in situ* stars on retrograde orbits at z=0. Most of the galaxies show a change in the orbits of the Splash population at the end of the MMAP accretion. However, there are a few galaxies in which this change in the orbits of Splash stars does not coincide with the end of the MMAP accretion but rather the end of another massive accretion event. These results provide good evidence that the Splash occurs due to the disruption of the disc caused by any kind of accretion event. For an alternate explanation for the Splash please see Amarante et al. (2020). In that work, they use hydrodynamical simulation of an isolated galaxy that develops clumps in high-density regions of the disc and also produces a bimodal disc. They find that the clump scattering forms a metal-poor, low angular momentum, population, without the need for a merger. Recently, Dillamore et al. (2023) looked for an alternate explanation for the high density of stars located in the same region as the Splash in the Energy-Angular momentum plane. They show such a population could be caused by the effects of bar resonance.

In this Chapter, we present a study of the chemodynamical properties of the Splash, as defined in Section 3.2.1. In Section 3.2.2.2 we discuss the corrections applied to the elemental abundances employed in this work for systematic effects as a function of surface gravity ($\log g$). The kinematic properties and spatial distribution of our Splash sample are described in Section 3.2.3, compared to the rest of the high-α disc. Our method for the analysis of the chemical properties of the Splash and disc populations is introduced in Section 3.3.1, and our results are presented in Section 3.4. In Section 3.5 we study how the chemistry and kinematics of the high-α disc are related, comparing them to zoom simulations of MW-like galaxies. We also examine the differences between simulated galaxies which have undergone GE/S-like massive mergers (GES) and those which only suffered minor mergers (MA). We conclude the chapter with a discussion and summary of our findings in Section 3.6.

3.2 Data & Sample

We make use of the 17th data release (DR17, Abdurro'uf et al., 2022) from the SDSS-IV/APOGEE-2 survey (Blanton et al., 2017; Majewski et al., 2017), along with distances and velocities based on *Gaia* eDR3 (Gaia Collaboration et al., 2021) and `astroNN`[1] (Leung & Bovy, 2019b). APOGEE is a near infra-red (H-band) spectroscopic survey based on both the northern and southern hemispheres. With the use of the 2.5m Sloan Foundation Telescope at Apache Point Observatory (APO, Gunn et al., 2006) in the United States (APOGEE-2N) and the 2.5m du Pont Telescope (Bowen & Vaughan, 1973) at Las Campanas Observatory in Chile (APOGEE-2S), APOGEE is able to achieve full sky coverage with data for over 650,000 unique targets. These telescopes are fitted with twin high-resolution (R $\sim$ 22,500) multi-fibre spectrographs (Wilson et al., 2019)

---

[1] https://github.com/henrysky/astroNN

providing abundances for over 20 different elements. Abundances are derived from the automatic analysis of spectra using the ASPCAP pipeline (García Pérez et al., 2016; Jönsson et al., 2020). For further details and information on data reduction and selection criteria, see Nidever et al. (2015); Holtzman et al. (2015, 2018); Zasowski et al. (2017); Beaton et al. (2021); Santana et al. (2021).

3.2.1 Sample selection

To get the best abundances we limit our parent sample to G-K giant stars. In addition, we only select primary main survey targets by setting the `EXTRATARG` = 0, and make some quality cuts to obtain our clean sample. Our selection criteria can be summarised as follows:

- $d_{\odot} < 3$ kpc
- $1 < \log g < 3$
- 4000 K$< T_{\rm eff} < 6000$ K
- SNR > 100
- $d_{\rm err}/d < 0.2$
- `ASPCAPFLAG` = 0
- `EXTRATARG` = 0
- $[X/Fe] > -10$ (X being each element used in the analysis)

The last criterion aims at removing stars for which a given elemental abundance could not be delivered by ASPCAP (listed in the catalogue as equal to -9999). We also remove all GC members included in the DR17 Value Added Catalogue (Schiavon et al. 2023, MNRAS, submitted). For the reasons exposed in Section 3.2.2.2, we restrict our sample to the solar neighbourhood by limiting the heliocentric distance to 3 kpc. In addition, since we are mainly concerned with the comparison between the Splash and the high-α disc, we adopt a chemical composition selection in order to isolate a clean high-α disc sample. That definition is made on the basis of the [Mg/Fe]-[Fe/H] plane, as shown in Figure 3.1. The resulting parent sample consists of 14,258 stars. A simple arbitrary eccentricity cut is then made to separate the disc and Splash populations, with any star of e $>$ 0.6 being defined as belonging to the Splash. We eyeball an eccentricity of 0.6 because this is where we see a turn-over in the gradient of the eccentricity distribution of the high-α disc from a normal Gaussian tail into a flat extended tail (See Figure 3.2).

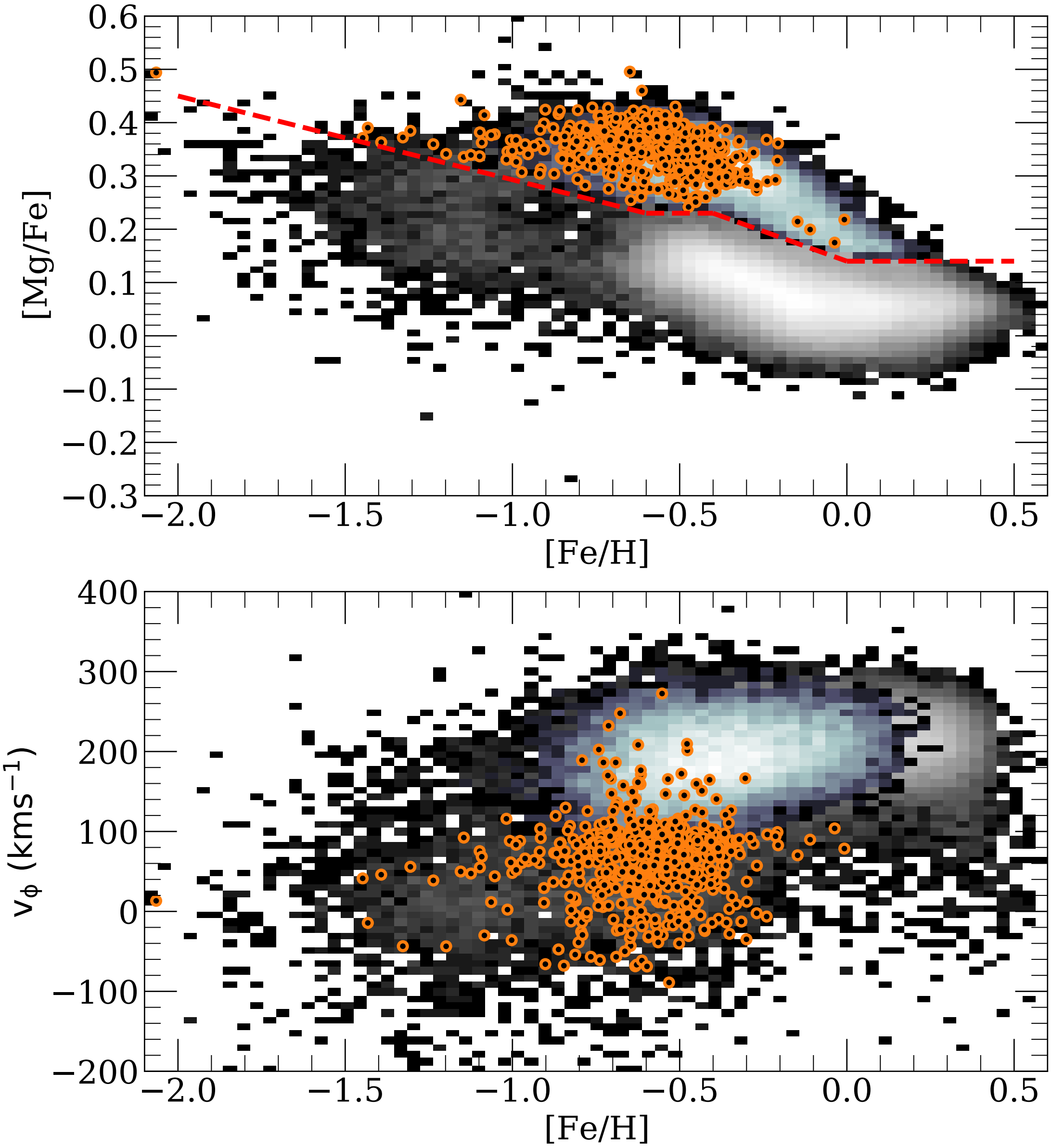

FIGURE 3.1: Both plots show the clean APOGEE data in the greyscale 2D histogram. Over-plotted are the high-α disc shown as the blue histogram and Splash as the orange dots, both limited to the solar neighbourhood, R < 3 kpc. A cut is made in the [Mg/Fe]-[Fe/H] to only select high-α disc stars, as shown by the red dashed line in the top panel. The bottom panel shows the tangential velocity against metallicity plot used in Belokurov et al. (2020); Belokurov & Kravtsov (2022) to define the Splash. Our selection places the Splash in the same locus as that of Belokurov et al. (2020).

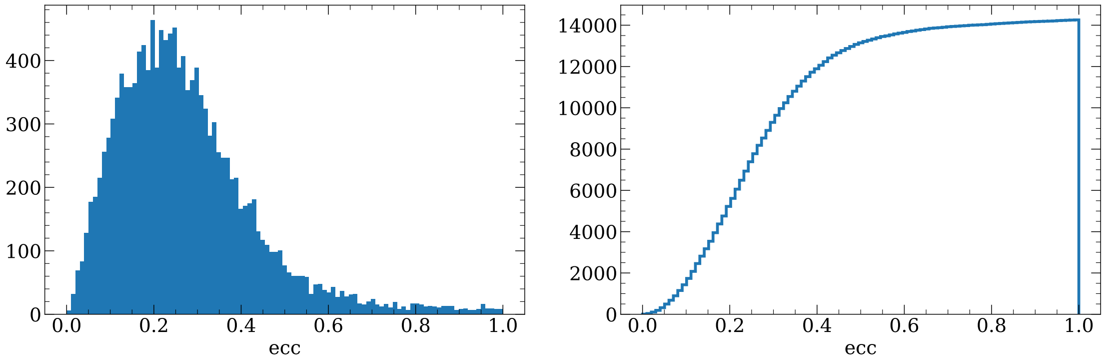

FIGURE 3.2: Eccentricity distribution for the high-α population. The left panel shows the histogram and the right panel shows the cumulative distribution. We select the Splash to be the upper tail end of this distribution where we see a change in the gradient, at e > 0.6.

3.2.2 Motive for our sample selection

3.2.2.1 Apogee selection function

By limiting our sample to the solar neighbourhood only, we may be missing out on a lot of information about the nature of the Splash as seen at the Galactic level. However, in addition to the reasons pointed out in Section 3.2.2.2, we are also limited by APOGEE's selection function. In Horta et al. (2021a), they point to the Splash population in the E-Lz plane, Figure 3.3, as the branch that extends from the disc locus at around $E \sim -1.8 \times 10^5$. However, as shown in Lane et al. (2022), this over-dense branch may be a result of the APOGEE selection function (see Figure 6 of Lane et al., 2022). By limiting our analysis to the solar neighbourhood, we minimise the potential effects of the selection function on our results.

3.2.2.2 Correction for abundance systematics

In recent papers, systematic trends of APOGEE abundances as a function $\log g$ have been reported by various groups (e.g., Eilers et al., 2022; Weinberg et al., 2022; Horta et al., 2023). Such systematics must be corrected to enable unbiased comparisons between samples of stars with different $\log g$ distributions. We perform this correction for each abundance individually adopting the following procedure. First, we fit a second-order polynomial to the distribution of the data in various [X/H]-$\log g$ planes. Second, we subtract the value of the polynomial from the median of the distribution to derive a residual correction to elemental abundances for a given value of $\log g$. Third, we add this difference to the original abundance ratios. Eilers et al. (2022) show that there is a significant bias in the $\log g$ distribution of stars depending on the distance at which they

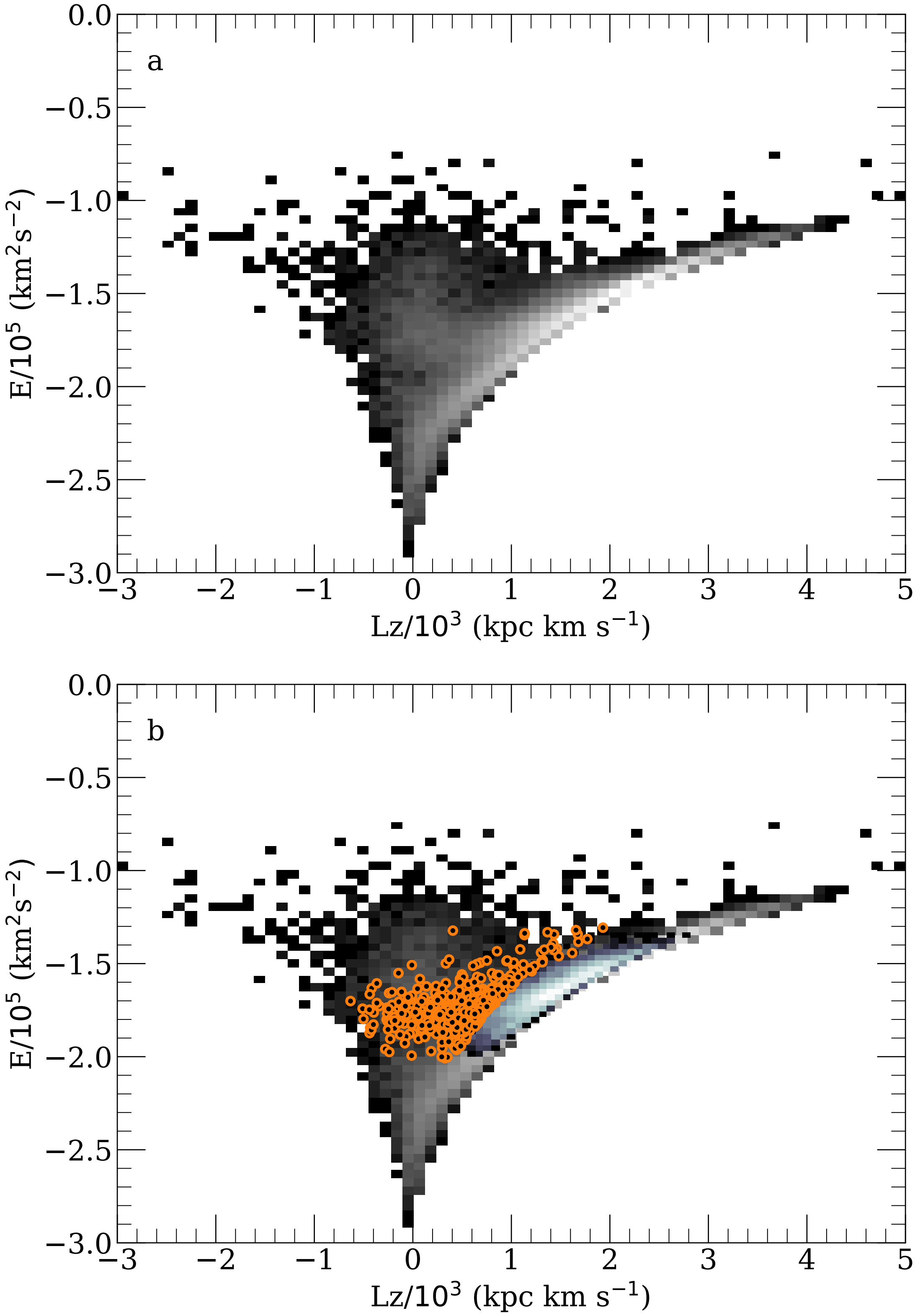

FIGURE 3.3: *top panel:* Energy-Angular Momentum plane to show a 2D histogram of stars in the APOGEE catalogue with the selection criteria described in Section 3.2.1. Positive Lz is prograde. The tuning fork feature is visible with a gap at ~ $(0, -2.0\times10^5)$. *bottom panel:* Same as the top panel but now highlighting the Splash (orange) and high-α disc (blue) selections in the solar neighbourhood only.

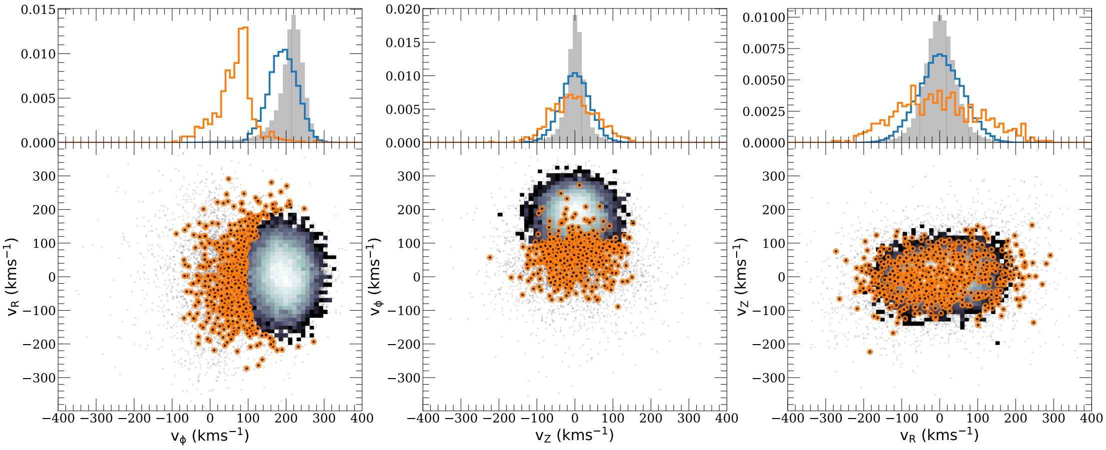

FIGURE 3.4: Velocity plots showing on the bottom/top panels the 2D/1D distributions of the Splash (orange dots/orange histogram), high-α disc (2D histogram/blue histogram) and the full clean APOGEE sample (black dots/filled grey histogram). The 1D histograms share the same x-axis as the plots below them. We can see from the left panels that there is a clear difference between the Splash and the high-α disc in v$_\phi$. For v$_Z$ and v$_R$ the 2D distributions for our two samples are very similar, however, the 1D histograms show the Splash to be slightly more extended in both velocities.

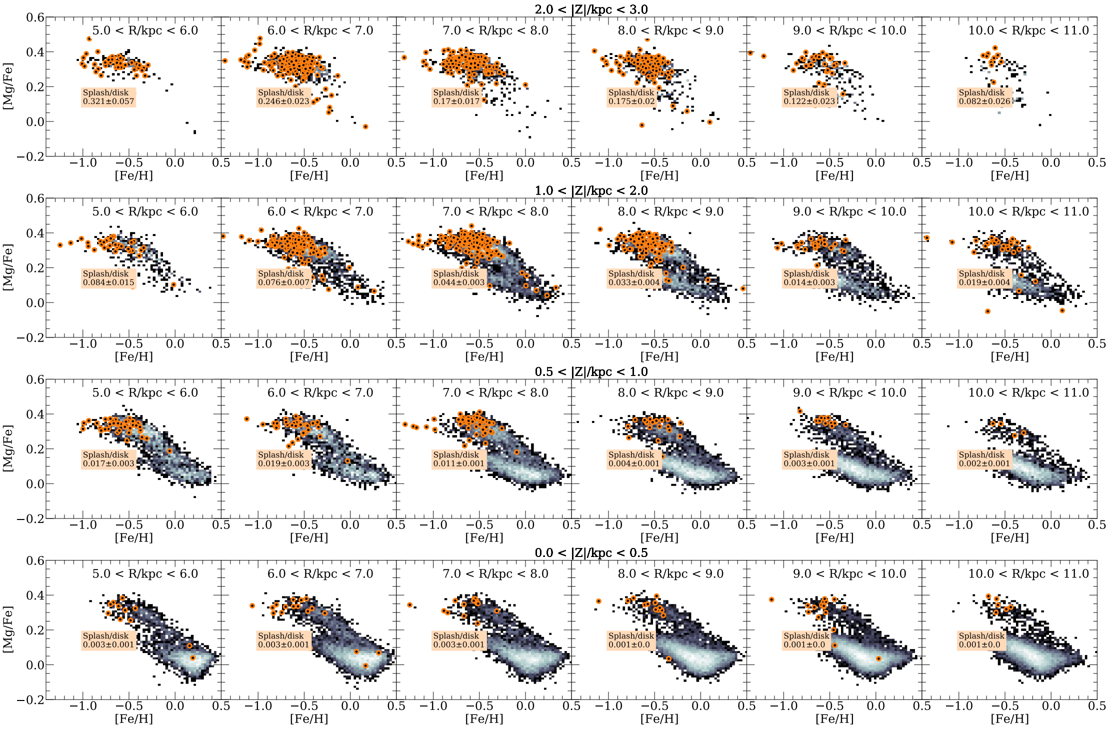

FIGURE 3.5: Distribution of the Splash (orange dots) and high-α disc (2D histogram) in the [Mg/Fe]-[Fe/H] plane as a function of Galactic radii (R/kpc) and absolute vertical height (|Z|/kpc). We also show the ratio of Splash to high-α disc in the metallicity range $-1.1 <$ [Fe/H] < -0.3, marked by black dashed lines, the errors for which are taken to be the standard error for the number of stars. The Splash fraction is seen to increase with increasing Z, but seen to decrease with increasing R. See Figure 3.6 for a better visual of this.

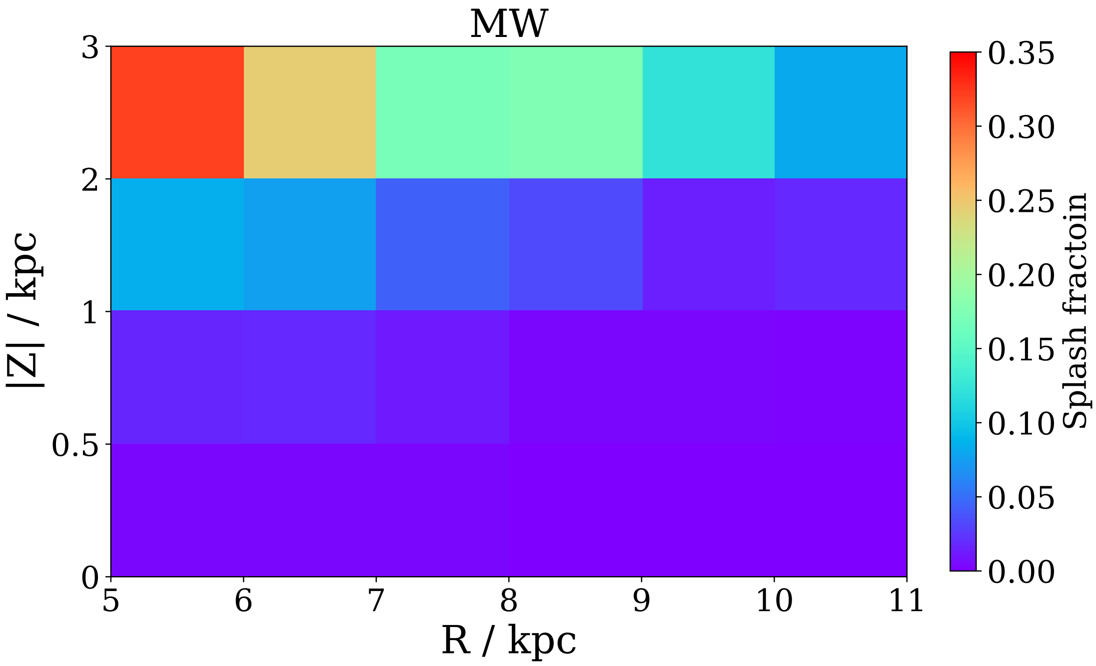

FIGURE 3.6: A confusion map showing the splash fraction of each panel from Figure 3.5. This shows us that the Splash fraction of the MW increases at higher values of Z and lower values of R.

are observed, with lower gravity stars being over-represented in more distant samples. By the same token, elemental abundances are known to vary as a function of position, so our correction for systematics as a function of $\log g$ could potentially erase such abundance gradients. To remedy this potential issue, we restrict our sample to a relatively small spatial distribution. Another way to minimise the effects of this systematic effect would be to select a narrower range of $\log g$, but that would reduce our sample to intolerably low numbers.

3.2.3 Kinematics and Spatial Distribution

In this section, we examine the velocities and positions of Splash and high-α disc stars, shown in Figures 3.4 & 3.5, respectively. The bottom panels of Figure 3.4 show the distribution of our sample stars in kinematic space (cylindrical coordinates). As in previous plots the orange dots represent Splash stars and the 2D histogram shows the distribution of the high-α disc stars. We also show in these plots the clean APOGEE sample, defined in Section 3.2.1, as small black dots in the background. The top panels display the distributions of the same sub-samples in the three components of the velocity vector, in the form of normalised 1-D histograms, adopting a consistent colour scheme. What quickly stands out in the first two bottom panels are the black dots that extend to lower tangential velocities than the Splash. We can see from the histogram of tangential velocity, in the top left panel, the majority of the APOGEE sample is at much higher values than the Splash, highlighting that these extended points are only a small fraction of the full sample. We know from previous studies that this is the GE/S system, along with other less evolved accreted systems (Helmi et al., 2018; Belokurov et al., 2018). This Figure illustrates clearly the kinematic differences between our sub-samples. The Splash is characterised by lower tangential velocity and a larger spread in both radial and vertical velocities, than the other sub-samples. These differences are entirely expected, given that our Splash sample is defined in terms of high eccentricity. By the same token, we find that the high-α component is characterised by a slightly lower tangential velocity and higher radial and vertical dispersion than the main APOGEE sample. This is also expected, that a large part of the Galactic disc is the younger low-α, or thin disc, population which on average is more circular than the older high-α population.

We next explore the spatial distribution of Splash stars, cast in terms of number counts as a function of position. Because our data are not corrected from the APOGEE selection function, we must devise a measurement that is not sensitive to selection effects. To minimise those effects, we anchor our Splash star counts on the number of their high-α disc counterparts, taking ratios within relatively small spatial bins. For this measurement only, we change the spatial cuts of our sample from a sphere around the Sun to an annulus of thickness 6 kpc centred on the Galactic centre, 5 kpc $<$ R $<$ 11 kpc and $|Z| < 3$ kpc, also including the low-α region of the [Mg/Fe]-[Fe/H] plane for comparison with the simulated galaxies presented in later sections. In Figure 3.5 we show the distribution of high-α and Splash stars on the [Mg/Fe]-[Fe/H] plane, in bins of Galactocentric distance (R) and vertical distance (Z) from the Galactic plane, in cylindrical coordinates. We adopt the same colour scheme as used in Figures 3.1, 3.3 and 3.4. As originally shown by Hayden et al. (2015), we find that, while the number of high-α disc stars varies greatly with position, those stars lie roughly on the same α-Fe plane locus across the Galactic disc. The number ratio between the Splash and the high-α disc stars, the Splash fraction, is shown in the insets within each panel. There is a clear trend of this ratio with respect to the vertical distance from the Galactic plane and radial distance from the Galactic centre: the further away from the plane the larger the contribution of the Splash. Moreover, the closer to the Galactic centre the higher the contribution of the Splash, which is in good qualitative agreement with predictions from Grand et al. (2020) (see their Figure 5). Figure 3.6 shows a confusion map of this Splash fraction in the MW for a better visual. While we do see the MW following the same trend as the predictions with respect to the radial distribution of Splash stars, it is not clear whether the predictions follow the same behaviour as the MW with respect to the vertical distribution. Grand et al. (2020) show the Splash to be more centrally concentrated than the disc but also extends to larger vertical heights. However, we must keep in mind that our sample is restricted to the solar neighbourhood, only reaching as close to 5 kpc from the galactic centre.

3.3 Chemistry of Splash vs High-α stars

In this section, we examine how these two populations compare in terms of their detailed abundance patterns. Our goal is to establish whether these two populations differ chemically, and how that comparison leads up to a better understanding of the origin of the Splash population. Figure 3.7 displays the two populations as a scatter plot in the [X/Fe]-[Fe/H] plane for all 16 abundance.

3.3.1 Method

We apply two different statistical methods to compare the chemistry of the Splash to the high-α disc populations. The first method consists in splitting our samples into bins of metallicity, [Fe/H], and calculating the average abundances for a selection of elements, similar to what is done in Horta et al. (2023) (see Section 3.3.2). The second is using a similar method as Taylor et al. (2022) to compute a χ^2 between the splash and the high-α disc and comparing this to the χ^2 obtained when comparing 1,000 bootstrap samples of the high-α disc to the whole high-α disc. Each of the 1,000 bootstrap samples has precisely the same size as that of the Splash sample (see Section 3.3.3).

Our comparison of the two populations covers the metallicity range $-1.1 < [\mathrm{Fe/H}] < -0.3$. The upper limit is due to the lack of more metal-rich Splash stars in our sample. That is due to the eccentricity cut adopted to define the Splash population, which selects against metal-rich stars. The lower limit is due to our definition of the Splash and high-α samples (Figure 3.1), which is aimed at minimising contamination by halo stars.

The elemental abundances adopted in our comparisons are the following: 1) α-abundance ratios: [O/Fe], [Mg/Fe], [Si/Fe], [S/Fe] and [Ca/Fe]. We also include a combination of these abundances by taking the inverse weighted average, which we label [α/Fe]. See Section 3.4.1.1. 2) light and odd-Z: [C/Fe], [N/Fe], [C+N/Fe], [Al/Fe] and [K/Fe]. For an indication of age, we also show [C/N]. See Section 3.4.1.2. 3) Iron-peak elements: [Cr/Fe], [Mn/Fe] and [Ni/Fe]. See Section 3.4.1.4. 4) s-process: [Ce/Fe]. See Section 3.4.1.5. Note that while we show the comparisons for elements that are a combination of others, [α/Fe], [C+N/Fe] and [C/N], we do not include them in the calculation used to obtain χ^2.

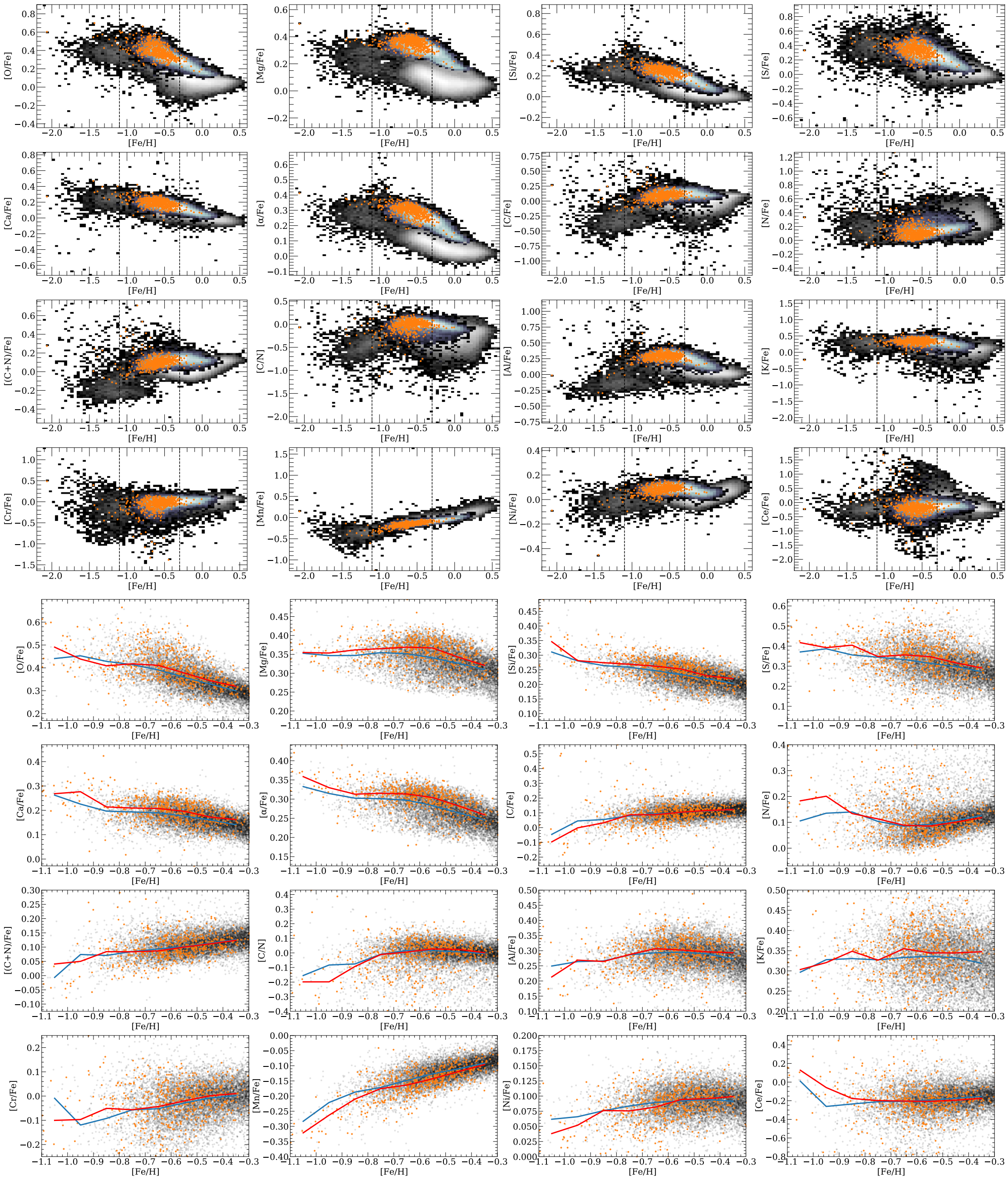

FIGURE 3.7: [X/Fe]-[Fe/H] planes for all abundance ratios analysed in Chapter 3. The first 16 panels show the full metallicity range covered by APOGEE. The grey 2D histogram shows the fully cleaned APOGEE sample, with the high-α disc stars shown as the blue 2D histogram and the Splash stars as the orange points. The bottom 16 panels zoom in to the metallicity range considered in Chapter 3. These panels show the Splash stars as orange points and high-α disc stars as black points. Also shown is the running median for both samples, red for the Splash and blue for the high-α disc stars.

3.3.2 Abundance comparison

For this first method, we follow a similar procedure as that used in Horta et al. (2023). We split our samples into bins of metallicity and compare the abundance ratios for all elements in each bin. Metallicity bins are chosen to have small enough widths to prevent any chemical evolution effects from affecting the sub-samples. The four [Fe/H] bins adopted are the following: [–1.1,–0.8], [–0.8,–0.6], [–0.6,–0.45], and [–0.45,–0.3]. Within each bin, median abundance ratios are computed for the two sub-samples. Errors are calculated through a method where we take 1,000 random bootstrap samples, with replacement, from our Splash and high-α disc samples, individually, then calculate the standard deviation of the median values of the 1,000 random samples.

Figure 3.8 delivers a visual rendering of the comparisons. Each panel shows the median value of each abundance for the two samples and their respective errors, providing a qualitative indication of similarities across the various abundance ratios. Quantitative estimates are obtained through computation of χ^2 differences, as follows:

$$\chi^2 = \sum_i \frac{(\overline{[\mathrm{X/Fe}]}_{i,\mathrm{Splash}} - \overline{[\mathrm{X/Fe}]}_{i,\mathrm{Disc}})^2}{\sigma^2_{[\mathrm{X/Fe}]_{i,\mathrm{Splash}}} + \sigma^2_{[\mathrm{X/Fe}]_{i,\mathrm{Disc}}}} \tag{3.1}$$

where $\overline{[\mathrm{X/Fe}]}$ is the median and σ is the standard deviation of the medians for the 1,000 random samples. Results are displayed in Figure 3.8, where both χ^2 and the corresponding probability for the two distributions being the same are shown at the top of each panel.

3.3.3 χ^2 distribution

Another way to check whether there is a difference or similarity between our Splash and high-α disc samples is by comparing the [X/Fe]-[Fe/H] relation in the two populations, for each element. This method was developed by Taylor et al. (2022). While in that paper the statistic adopted was the difference between the abundances in two populations, here we focus on the χ^2. This will give us an idea of which elements show the largest differences across the full metallicity range of our sample. To calculate the χ^2, for each abundance ratio, we split our samples into ten bins so that each bin consists around 60 Splash stars. Each bin has a size that is at least twice the average measurement error of stars within. The metallicity bins adopted are the following: [–1.1, –0.8], [–0.8, –0.71], [–0.71, -0.65], [–0.65, –0.62], [–0.62, –0.58], [–0.58, –0.54], [–0.54, –0.51], [–0.51, –0.47],

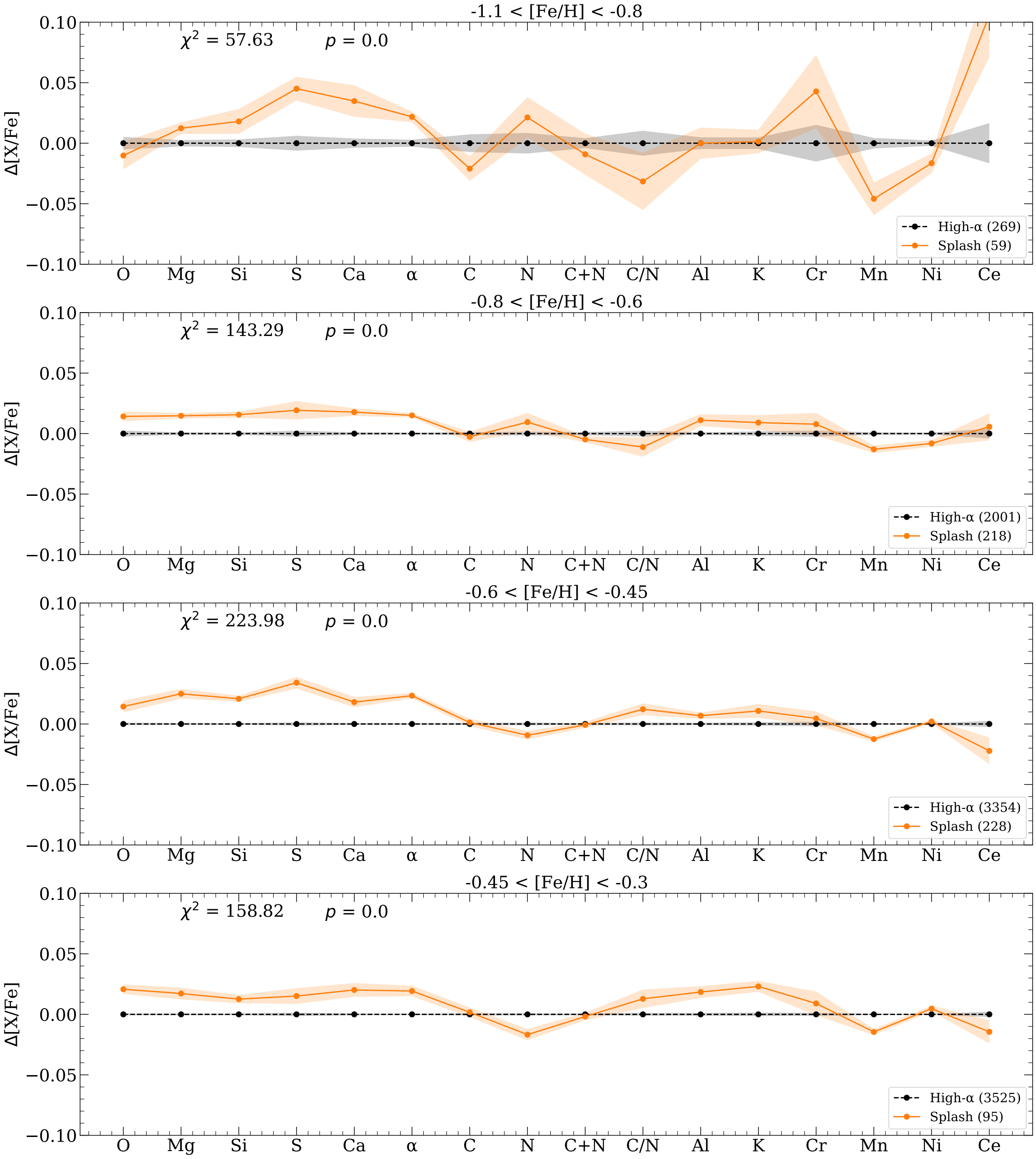

FIGURE 3.8: The chemical comparison plot between the Splash and the disc, the results for which are laid out in Section 3.4.1. The points show the median values, orange for Splash and black for high-α disc, with the medians of the high-α subtracted from both, hence the black points all lie on zero. The shaded regions are the respective 1σ errors calculated using the method described in Section 3.3.2. The number of stars in each bin is shown in brackets in the legend. Also shown are the χ^2 and p-value for the comparison between the two samples in each panel. We see a clear difference between the Splash and the high-α disc across all metallicity bins. Noteworthy is the differences in the α-abundances with Splash having higher abundance ratios for each α-abundances, suggesting it is an older population. We also point out the difference in Mn, an iron-peak element, with the Splash having lower [Mn/Fe] across each metallicity bin, suggesting again that it is older than the high-α disc

[–0.47, –0.41], [–0.41, –0.3]. We then compute the χ^2 using the following equation:

$$\chi^2 = \sum_i \frac{(\overline{S_i} - \overline{D_i})^2}{\sigma_{S_i}^2 + \sigma_{D_i}^2} \tag{3.2}$$

where $\overline{S}$ and $\overline{D}$ are the median abundance ratios of the Splash and high-α disc, respectively, per metallicity bin, i, and σ is the standard error calculated as the standard deviation divided by the square root of the number of stars, $\frac{std}{\sqrt{N}}$. To aid in the interpretation of the χ^2 values, we compare them with the null hypothesis estimated from the calculation of χ^2 values obtained from the comparison of high-α disc stars with randomly selected samples of the same population. In other words, we repeat the χ^2 calculation but now replacing the Splash stars with random same-sized samples of high-α disc members. This is done 1,000 times following the bootstrap method, which gives us a distribution of χ^2 peaking at the value which is most similar to the whole high-α disc sample. So, any χ^2 value obtained from the Splash and high-α disc comparison which deviates from the random sampled distribution has a clear difference in abundance across most of the metallicity range in which we compare, these are shown in Figure 3.9.

3.4 Results

In this section, we present the results for the two methods used to compare the Splash with the high-α disc. The results of the first method are discussed in Section 3.4.1 and the results for the second method in Section 3.4.2.

3.4.1 Abundance comparison results

In this section, we analyse the results obtained from the first method described in Section 3.3.2. The results are displayed in Figure 3.8 where the points represent the median values of the Splash (orange) and high-α disc (black) for the respective abundance ratios within each metallicity bin, specified on top of each panel. We also show as the shaded region the respective 1 σ error obtained from 1,000 bootstrapped samples. The χ^2 value obtained from comparing the elements of the two populations per metallicity bin is shown in each panel, along with the respective probability that the two populations are extracted from the same parent sample. We find that across all the metallicity bins there is a significant difference between the two populations, which is highlighted by the large χ^2 and zero probability. This suggests the Splash is chemically a separate and distinct population from the high-α disc. It is important to acknowledge here the possible contamination of our samples by low-α stars given our selection criteria. The majority of this contamination would occur in the high-α population, and in turn would increase the differences we see, mainly for the α-abundances. We look at the comparisons for each element in the following sub-sections.

It is essential that we emphasise the high quality of APOGEE data, which makes possible the measurement of very small chemical composition differences between two distinct populations. This capability is due to the combination of the high quality of the APOGEE data on a star-by-star basis (high S/N, moderately high-resolution spectra, obtained with two twin, single-configuration, exceedingly stable spectrographs) with the targeting of a very large and homogeneous sample. The latter is a very important aspect of the survey. After cleaning from contamination by foreground dwarfs (and to a much lesser degree AGB stars, wherever possible and necessary), the APOGEE main sample consists entirely of first-ascent red giants and red-clump stars. Objects in these evolutionary stages cover a relatively narrow range of effective temperature, surface gravity, and microturbulent velocity. Such a state of affairs simplifies spectral analysis tremendously, minimising errors due to uncertainties in model atmospheres and line opacities, and ultimately leading to the generation of a massive database of stellar parameters and chemical compositions of unparalleled precision.

3.4.1.1 α-abundances

First, we look at the comparison of the α-abundances between the Splash and high-α population, the first five elements on Figure 3.8, as well as the combination of them all, [α/Fe]. The abundance ratio [α/Fe] effectively measures the relative contribution of SNe II and SNe Ia to the gas that a star formed from. This is because α-element enrichment originates from the explosions of massive ($\geq 8\ \mathrm{M}_{\odot}$) stars which undergo core collapse. Due to the very short lifetimes ($\tau_{\star} \simeq 3-30$ Myr) of these progenitors, the delay time distribution (DTD, distribution of times between star formation and the likely time of some event) of SNe II for a burst of star formation is very narrow (see Figure 1 of de los Reyes et al., 2022). As a result, SN II are thought to initially dominate chemical enrichment and thus being strongly tied to ongoing star formation. Unlike SNe II, type Ia SNe are not thought to occur so promptly following star formation. This is because the delay time distribution of SNe Ia is set by the timescales of both stellar and binary evolution as their progenitors are intermediate-mass stars undergoing mass transfer. This results in a much broader range of delay times (Graur et al., 2014), so that SNe Ia are thought to dominate Fe-enrichment at later times, contributing minimal α-elements.

Consequently, the relation between [α-Fe] and [Fe/H] is a useful diagnostic of a galaxy's history of star formation and chemical enrichment. It is expected that for an extended history of star formation, it should be characterised by a flat sequence of [α/Fe] at low [Fe/H] connected to a declining sequence of [α/Fe] at high [Fe/H] by a so-called 'α-knee'. The knee is thought to indicate the point in the chemical enrichment history when SNe Ia begin to dominate and thus its absolute value in [Fe/H] is thought to constrain the early star formation rate. The slope of a sequence in the α-Fe plane reflects the balance between enrichment by SNe II and SNe Ia. A zero-slope, horizontal plateau reflects the IMF-averaged yield α-elements and Fe contributed by SNe II *only*. For the same reason, the slope of the shin reflects an increase in the contribution by SNe Ia, indicating how efficiently outflows act to remove metals from the ISM (Tolstoy et al., 2009; Andrews et al., 2017; Mason et al., in prep.).

For the full range of metallicities within which we run our comparisons, we see a clear difference between the Splash and high-α populations. The Splash is seen to be higher than the high-α disc for all α-abundances across all metallicity bins, with the exception of [O/Fe] in the lowest metallicity bin. A higher value of α-abundances in the Splash indicates an older population. This result is in line with other works (Gallart et al., 2019; Belokurov et al., 2020; Grand et al., 2020; Xiang & Rix, 2022) and supports the hypothesis that the Splash is the early heated disc. However, could there be an alternative mechanism, other than heating by a single accretion event, which would result in the higher α-abundance ratios of the Splash? We explore this question in Section 3.5.

3.4.1.2 Carbon & Nitrogen

C and N abundances of stellar populations are useful diagnostics of the chemical evolution of a galaxy. The largest contributors of C and N to the ISM are massive stars which explode as SNe II, followed by asymptotic giant branch (AGB) stars which form from intermediate-mass progenitors ($M \simeq 1 - 11$ M$_\odot$ (AGB through SAGB; Renzini & Voli, 1981a; Siess, 2010; Karakas, 2010). As stars evolve along the RGB, the stellar envelope puffs up and is shed (see Wiersma et al., 2009, and references therein). Prior to being shed into the interstellar medium, the stellar envelope is enriched in the products hot-bottom burning, by convective dredge up (Renzini & Voli, 1981a). Therefore abundances of C and N of a stellar population can reflect both contributions by SNe II *and* AGBs with different lifetimes.

The differences in [C/Fe] and [N/Fe] are not as clear cut as what we see for the α-abundances. For [C/Fe], there is a strong difference at the lowest metallicity bin, but the difference is not significant in the other bins. On the other hand, while [N/Fe] is significantly different in all metallicity bins, it goes from being higher in the Splash within the lower metallicity bins to higher in the high-α stars within the two most metal-rich bins. By combining [C/Fe] and [N/Fe] we provide the comparison of [(C+N)/Fe] which minimises the effect of CNO mixing. This abundance ratio does not exhibit a significant difference in any of the metallicity bins. We also show the [C/N] ratio to help provide an indication of the relative ages of the two populations, since it is observed that [C/N] correlates with age (e.g., Martig et al., 2016). However, the reliability of this correlation at low metallicities is poor. In the higher metallicity bins, we see that the Splash shows higher [C/N] ratios than the high-α disc which indicates that at these metallicities it is an older population. To fully understand the result across all metallicity bins a chemical evolution model of [C/N] against [Fe/H] for two systems, one with an early quenched star formation and another with an extended star formation, is required.

3.4.1.3 Odd-Z elements

Odd-Z elements, such as aluminium, are mostly synthesised by hydrostatic burning in massive stars and are released into the ISM by SNe II. At low [Fe/H], the Milky Way's *in-situ* populations and satellite galaxies show similar sub-solar odd-Z abundance ratios. At [Fe/H]$\gtrsim$–1, however, dwarf galaxies have characteristically depleted abundance ratios and the Milky Way generally shows super-solar abundance ratios (see, e.g., Tolstoy et al., 2009, and references therein). This can be explained by a combination of the metallicity-dependent yields of odd-Z elements with a higher and more extended history of star formation of the Milky Way than those of its satellites. Much work has been done to characterise the accreted substructures of the Milky Way using odd-Z abundances(e.g. Hawkins et al., 2015; Das et al., 2020; Horta et al., 2021a; Hasselquist et al., 2021; Fernandes et al., 2023).

The two odd-z elements for which we make a comparison are aluminium and potassium. Both [Al/Fe] and [K/Fe] show a very similar trend between the Splash and high-α populations. Other than the lower metallicity bin, where the two populations are the same for these abundance ratios, the Splash consistently has a higher abundance than the high-α population and the difference increases at higher metallicities. The trend we see here indicates that the Splash is an older population due to the higher contribution from massive stars. A high value for [Al/Fe] supports the notion that the Splash does not originate from a dwarf galaxy.

3.4.1.4 Iron-peak

The Fe-peak elements (e.g. Mn, Fe & Co) are contributed to the ISM by both SNe II and SNe Ia (e.g. Portinari et al., 1998; Iwamoto et al., 1999, respectively). In terms of the yields, the relative contribution of SNe II and SNe Ia varies in each case such that comparison of the abundance ratios of the other Fe-peak elements compared to Fe can help constrain the importance of each channel as well as the star formation history of a system. A thorough discussion of the importance of these comparisons can be found in Horta et al. (2023).

For the iron-peak elements we mainly focus on Mn and Ni, but also show the results for Cr. Throughout the whole metallicity range the [Mn/Fe] ratio is lower for the Splash, by a significant amount, which agrees with what we see in the alpha elements that the Splash is a less evolved population than the comparatively lower eccentricity high-α disc. For Ni, while at the lower metallicity, it is lower for the Splash, at higher metallicities there isn't a significant difference between the two populations.

3.4.1.5 Cerium

Neutron capture elements ($Z \gtrsim 30$) are formed by the capture of neutrons by the nuclei of the Fe-peak elements. Depending on the relative timescales of neutron capture and β-decay, such elements are termed slow or rapid (s- or r-) process elements. s-process elements originate from the atmospheres of intermediate-mass stars during the AGB phase of their stellar evolution, the most massive such progenitors have lifetimes on the order of 100 Myr.

From APOGEE we have only one s-process element with reliable abundance ratios, Ce. In our comparison, Ce does not show a clear trend between the Splash and high-α population. The Splash shows higher abundances ratios at the lower two metallicity bins, whereas the high-α disc shows higher abundances ratios at the higher metallicity bins. This result is in agreement with the others, showing that the star formation in the high-alpha disc is more extended than in the Splash evidenced by the higher AGB contribution.

3.4.2 χ^2 distribution results

In this section, we show the results for the second method used to compare the Splash and high-α disc, as described in Section 3.3.3. This statistic compares the relation

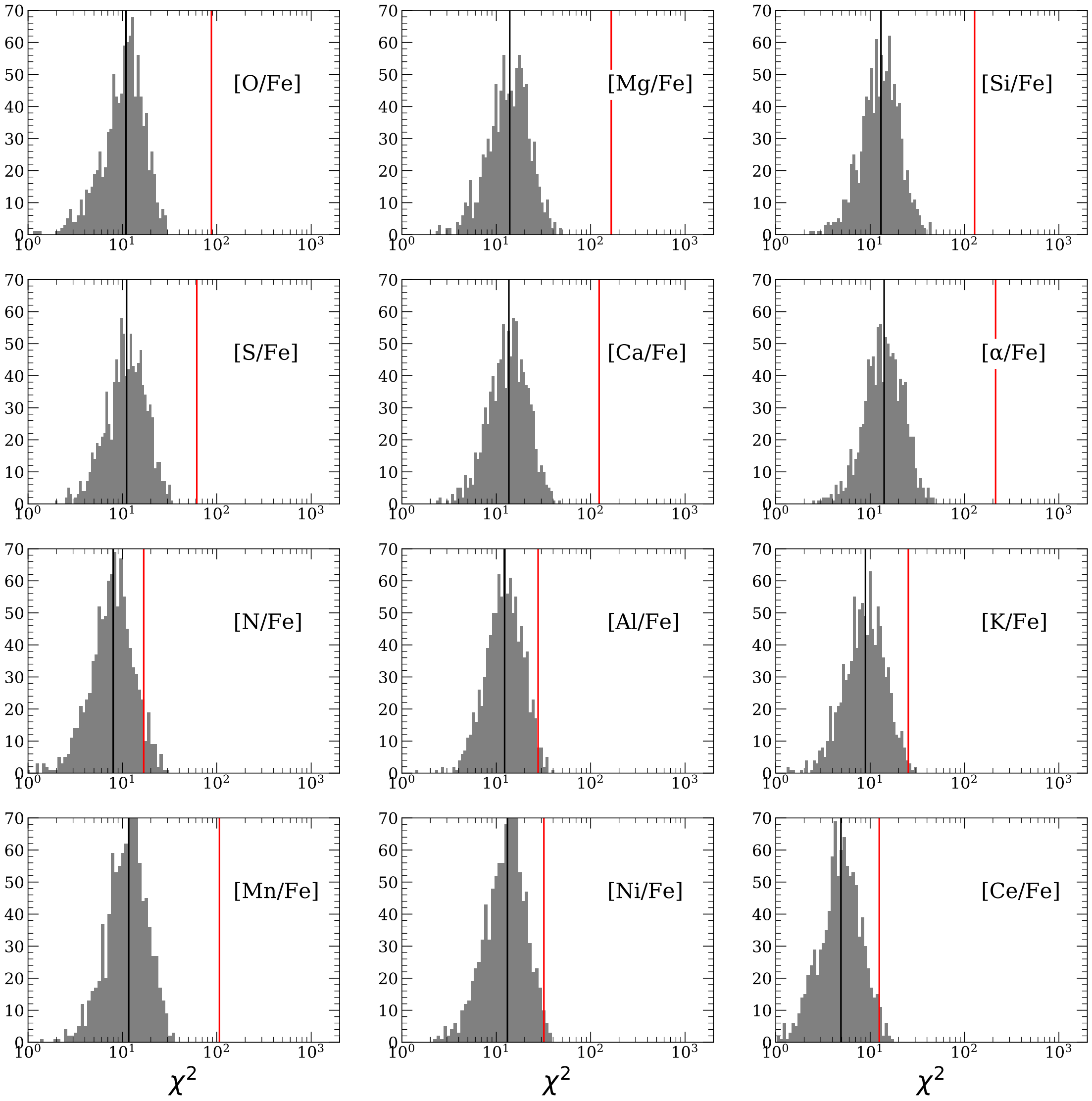

FIGURE 3.9: Comparison of χ^2 between the Splash and high-α disc (red line) compared to the distribution of χ^2 obtained from a random sample of the high-α disc (grey histogram), with the median of the distribution shown as the black line. See Section 3.3.3 for a full description and Section 3.4.2 for interpretation. Only showing here the abundances for which the difference in χ^2 for the Splash compared to high-α disc is large. All the α-abundances show a difference between the Splash and the disc which confirms the result in the previous section. We also see differences for N, Al, K, Mn, Ni and Ce.

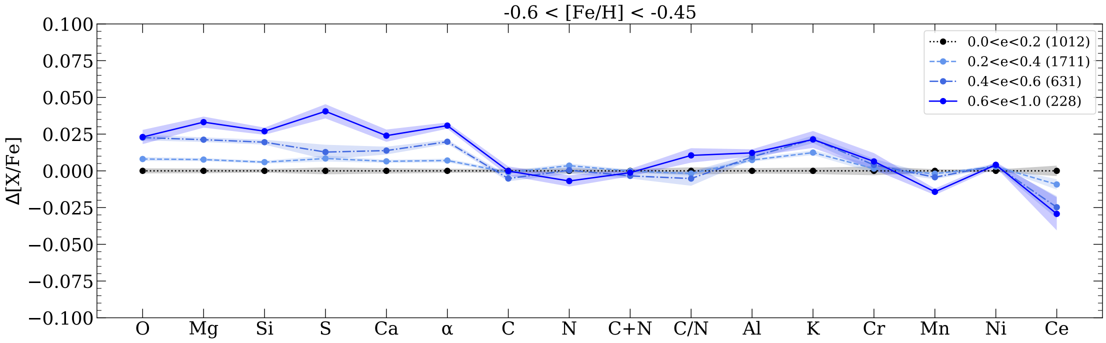

FIGURE 3.10: Similar to Figure 3.8 but with the high-α disc split into three eccentricity bins of size 0.2, only showing the metallicity bin with the largest sample. The lowest eccentricity bin ranging $0.0 < e < 0.2$, shown in black, is subtracted from the others, including itself, which is why it is placed at a Δ[X/Fe] of zero. There is a clear trend for some of the abundances with eccentricity, for example, most of the alpha abundances increase with eccentricity whereas Mn decreases. Though not shown, these trends are stronger at higher metallicities. In most cases the Splash ($0.6 < e < 1.0$) has the most extreme abundances.

between the abundance ratio of a given element, [X/Fe] and [Fe/H]. The statistic corresponding to the null hypothesis is estimated by running a comparison between 1,000 randomly selected disc samples with their parent population. Figure 3.9 shows only those abundance ratios for which the difference in χ^2 is large. The χ^2 value for the comparison between the Splash and the high-α disc is shown as the red vertical line and the median of the distribution is shown as the black vertical line. The large difference between the chemistry of the Splash and high-α is seen for 12 out of the 16 abundance ratios which we compare. There is a clear difference for all of the α abundances shown, as well as a high difference in Mn, which highlights the distinction in the evolutionary stages of the two populations. We also see smaller but significant differences in N, Al, K, Ni and Ce. This method of checking the differences between our two populations enhances what we find in Section 3.4.1, with the Splash having statistically older chemistry than the high-α disc. Our results highlight the level at which we can carry out statistical analysis to perform chemical tagging with such large data sets. For example, in the [Al/Fe]-[Fe/H] plane for the Splash and high-α (see Figure 3.7) it is difficult to distinguish a large difference with the eye. However, with such a large high precision data set we are able to statistically analyse them to measure the difference.

3.5 Answers in simulations

In this Section we attempt to answer the question: is the Splash really a separate system that stands out from the rest of the disc, as suggested by the results from the previous Sections, or are the chemical differences found as a result of the criterion adopted to

Comparison	$-1.1 < [\mathrm{Fe/H}] < -0.8$	$-0.8 < [\mathrm{Fe/H}] < -0.6$	$-0.6 < [\mathrm{Fe/H}] < -0.45$	$-0.45 < [\mathrm{Fe/H}] < -0.3$
$0.0 < e < 0.2$ vs. $0.2 < e < 0.4$	12.02 (0.44)	46.37	105.77	52.4
$0.2 < e < 0.4$ vs. $0.4 < e < 0.6$	22.1 (0.11)	118.81	215.01	142.48
$0.4 < e < 0.6$ vs. $0.6 < e < 1.0$	57.34	55.06	76.4	56.96

TABLE 3.1: χ^2 comparison between each eccentricity bin for adjacent metallicity bins. Non-zero p-values shown in brackets.

define the Splash? Correlations between chemical composition and kinematics are known to exist (Mackereth et al., 2019; Belokurov et al., 2020; Horta et al., 2021a), so it is possible that the chemistry of our Splash sample is simply the result of an extension to high eccentricity of the abundance trends with kinematics present in the high-α disc population. If the scenario in which the Splash is caused by the merger with GE/S is true, there should be some kind of a signature in the relationship between chemistry and kinematics.

This hypothesis is tested by performing the same calculations described in Section 3.3.1 this time splitting the high-α sample into four eccentricity bins. The highest eccentricity bin corresponds to the Splash population. The results are shown in Figure 3.10. We focus only on one metallicity bin here, the one containing the largest number of stars. The results for other bins are mostly consistent with the metallicity bin shown in Figure 3.10, except for three elements, N, Cr and Ce. While Cr and Ce are a bit more sporadic, they do not show the same trend with respect to eccentricity in all metallicity bins, N shows a positive correlation with eccentricity at the lower two bins and a more negative correlation at the higher bins. We also show in Table 3.1 the χ^2 values, and the associated non-zero p-values, for the comparison between adjacent eccentricity bins. When looking at the chemical comparison we see correlations between abundance and eccentricity for some elements, mainly the α-abundances and Mn. We observe for α-abundances a clear positive correlation with eccentricity, which indicates that if stars with higher α-abundances are older then there is an age correlation with eccentricity for the high-α disc of the Galaxy. This correlation is also observed in Belokurov et al. (2020) where they show the v_ϕ – [Fe/H] plane coloured by median [α/Fe] and median age. They find that both the median [α/Fe] and median age correlate with v_ϕ in the thick disc region of this plane, with the Splash being the low-angular-momentum part of the thick disc and therefore older than the disc. However, given that the Splash is proposed to result from a single catastrophic event, one would perhaps expect a more abrupt change in the correlation between chemistry and eccentricity when transitioning from the disc to the Splash due to the interaction with GE/S. The question remains, does the Splash require a massive GE/S-like merger or if it could potentially arise from comparatively less massive minor mergers? We look to the `ARTEMIS` simulations to help answer this question.

3.5.1 ARTEMIS

`ARTEMIS` is a suite of 45 zoom-in hydrodynamical simulations of Milky Way-mass galaxies run in a WMAP ΛCDM cosmological model. These are described in detail in Font et al. (2020), so here we provide a short summary.

The simulations were run with the Gadget-3 code (last described in Springel 2005), using the same hydrodynamics solver and subgrid physics as in the EAGLE simulations (Schaye et al., 2015; Crain et al., 2015), but with a recalibrated stellar feedback scheme that better matches the observed stellar mass–halo mass relation (see Font et al. (2020) for details). The mass of each dark matter particle is $1.17 \times 10^5 \mathrm{M}_\odot h^{-1}$, while the initial baryon particle mass is $2.23 \times 10^4 \mathrm{M}_\odot h^{-1}$. The total galaxy masses of the Milky Way-like haloes range between $0.8 < \mathrm{M}_{200}/10^{12}\,\mathrm{M}_\odot < 1.2$, where M_{200} is the mass enclosed within a volume of mean density 200 times the critical density at redshift $z = 0$. The `ARTEMIS` simulations match a broad range of properties of Milky Way-mass galaxies (e.g., stellar masses, luminosities, and metallicity distributions) and of their satellite dwarf populations (e.g. abundances, radial profiles or quenched fractions), as described in previous studies (Font et al., 2020, 2021, 2022).

In addition, the merger trees for all Milky Way-mass hosts have been constructed using the methods of McAlpine et al. (2016).

3.5.2 Sausaged (GES) and Sausageless (MA) galaxies

We select four MW-like galaxies, G29, G30, G34 and G42, that have had a GE/S-like merger event at an early time, which we call "Sausaged" galaxies, as well as three MW-like galaxies, G17, G19 and G44, that had more minor mergers with the MMAPs merger being around the same time as GE/S, called "Sausageless". For further insight into the nature of these simulated galaxies, see Dillamore et al. (2022). We aim to check whether there is a difference between the *in situ* population of the Sausaged and Sausageless galaxies. To check how these results match up to the observations we study only the 'solar neighbourhood' in the simulations defined as $|Z| < 3$ kpc and $5 < R < 11$ kpc, both in galactocentric cylindrical coordinates, which gives us an annulus of size 6 kpc. We also limit the metallicity to $[\mathrm{Fe/H}] > -2.5$ to best match the properties of our sample.

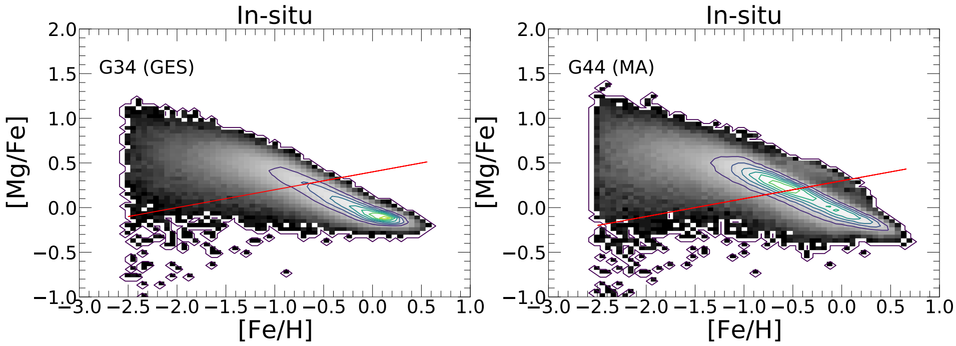

FIGURE 3.11: Examples of our selection for high-α disc in the [Mg/Fe]-[Fe/H] plane for our simulated Sausaged galaxy (G34, left) and a Sausageless galaxy (G44, right). Anything above and to the left of the red line is defined as high-α. The selection is made only for the *in situ* population which is shown as the 2D histogram. Also shown are the contours for the *in situ* population which helps us draw the dividing line between high- and low-α.

3.5.2.1 Qualitative comparison

For a qualitative test, we inspect the relationship between the chemistry and kinematics, focusing on the clear correlation we see between the α-abundances and eccentricity in the high-α disc. An investigation of the simulations has the added bonus of being able to establish unequivocally which stars are accreted or *in situ*. To select the high-α disc in the simulated galaxies we make a simple cut to the *in situ* population in the [Mg/Fe]-[Fe/H] plane of each galaxy to best mimic how we separate the high- and low-α discs with APOGEE. To do this we remove the high-density region at low [Mg/Fe] and high [Fe/H], which we associate with the low-α disc. We show in Figure 3.11 this selection for two of the galaxies, G34 a Sausaged galaxy and G44 a Sausageless galaxy. In Figure 3.12 we plot the [Mg/Fe]-Lz distribution for our high-α population, of our two galaxies mentioned above as well as the MW for comparison, to show the gradient between chemistry and kinematics. We use angular momentum rather than eccentricity because it is more easily calculated in the simulations and also correlates very well with eccentricity, with Lz=0 having high eccentricity and larger |Lz| having lower eccentricity. Examining the running median, shown as the red line, we can see a clear correlation between [Mg/Fe] and Lz for both the Sausaged and Sausageless galaxy, with not much of a qualitative difference between the two. This is also the case for all the other simulated galaxies that are analysed. Note the higher abundance of retrograde stars in the G44 compared to G34, we further examine this in the following section. From this analysis, we see that there is no qualitative difference between Sausaged and Sausageless galaxies with respect to correlations between chemistry and kinematics. However, a comparison between simulated galaxies and the MW shows an intriguing result. Simulated galaxies display a very large number of retrograde stars, much larger, relatively, to what is found in the APOGEE data for the Milky Way. Moreover, the simulated galaxies show a kink in the relation between abundance ratios and kinematics at the transition between retrograde to prograde stars, which is not seen in the observational data.

3.5.2.2 Quantitative comparison

To put a number to the Splash fraction between Sausaged and Sausageless galaxies, we define the Splash in a way that can consistently be applied to all of our simulated galaxies without a biased selection. To do this we define the Splash as anything that is tagged as *in situ* and has a retrograde orbit ($Lz < 0$) at a redshift of 0, following a similar definition as Dillamore et al. (2022). We then take the ratio between the *in situ* retrograde and prograde populations to give the Splash fraction. Also, to check whether there is a relation with where you observe in the galaxy we split our 'solar neighbourhood' annulus into six sections and calculate the Splash fraction in each section.

We plot our findings in Figure 3.13, where each point is the Splash fraction, per section, coloured by simulated galaxy. The error bars are the error associated with the fraction. The Splash fraction is plotted against the accreted retrograde fraction as a test to assess the impact of the orbital properties of the accreted system on the Splash. The galaxies labelled GES are the Sausaged galaxies and those labelled MA (minor accretion) are Sausageless.

What straightaway stands out is the linearity between the Splash fraction (again, defined as the *in situ* retrograde fraction) and the accreted retrograde fraction. Comparing the Sausaged and Sausageless galaxies, on average the Sausaged galaxies have a higher Splash and accreted retrograde fractions. However, we can see that the mass ratio of the MMAP is not the only parameter determining the splash fraction. For example, one of the Sausageless galaxies, G44, has a higher Splash fraction than two of the Sausaged galaxies. This is likely due to the number of merger events being greater in G44 and the mergers occurring on more retrograde orbits. Inspecting each galaxy individually, split into six sections, we see that the Splash fraction varies significantly from section to section. Interestingly, the two sections of G44 that have high fractions are situated opposite each other. This could provide information about the shape of the Splash. Another interesting point to highlight from Figure 3.13 is the grouping of the three galaxies around (0.04,0.07) which show a large scatter in the relation. We speculate the cause of this in Section 3.6.

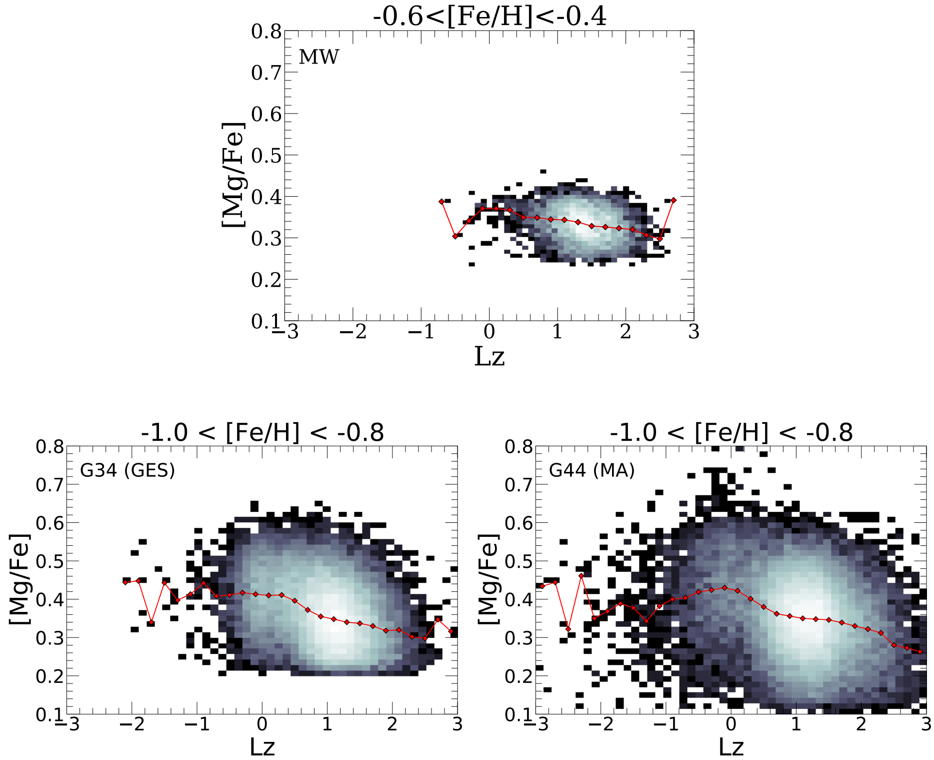

FIGURE 3.12: *top panel:* The [Mg/Fe]-Lz plot for the MW's high-α disc within the metallicity range $-0.6 <$ [Fe/H] < -0.4. *bottom panels:* The same galaxies as Figure 3.11 in the [Mg/Fe]-Lz plane, also only showing the high-α population as a 2D-histogram. The metallicity is restricted to a narrow range to avoid any evolutionary biases. The red line is the running median, showing the correlation between [Mg/Fe] and Lz.

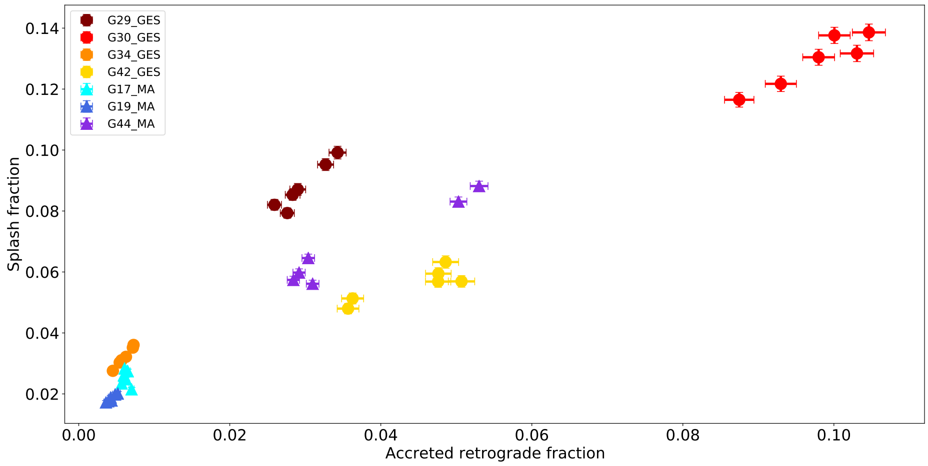

FIGURE 3.13: Showing the Splash fraction vs accreted retrograde fraction for each of the 6 sections of the simulated galaxies. Each colour represents one galaxy with the associated error bars. Dots represent Sausaged galaxies and triangles represent the Sausageless galaxies. This plot shows a strong positive correlation between these two variables.

3.6 Discussion

The results we present in this chapter make use of observational data from APOGEE as well as the `ARTEMIS` simulations to help constrain the origins of the Splash population. The APOGEE data allow us to make a comparison between the Splash and the rest of the high-α disc for 16 different chemical abundance ratios, as well as study the distribution of stars in the solar neighbourhood in a way that minimises the effects of the selection function. These results along with the analysis of the simulations give us a clearer picture of how to tackle the problem of understanding the true origin of the Splash.

So far in the literature, there has been a large focus on studying the Splash in the context of it being the result of the merger with GE/S (Gallart et al., 2019; Grand et al., 2020; Belokurov et al., 2020; Belokurov & Kravtsov, 2022; Xiang & Rix, 2022; Ciucă et al., 2023; Lee et al., 2023). One of the main questions in this chapter is to ask whether there is chemodynamical difference between galaxies that have undergone a GE/S-like merger (Sausaged) and those without (Sausageless). Simulations have shown that a GE/S merger results in a Splash-like population forming (Grand et al., 2020; Belokurov et al., 2020). Naturally, these results prompt the question of whether the Splash can be formed outside of a GE/S-like merger. This question is partially answered in Dillamore et al. (2022), where they find that discs are perturbed due to high mass mergers but not only the MMAP. In this chapter, we add to the work by Dillamore et al. (2022) and show that there are no strong chemodynamical differences between Sausaged and Sausageless galaxies.

From the results obtained on the basis of APOGEE, we find that our simple selection of the Splash agrees with previous works and kinematically behaves as expected, as a halo-like component, considering our selection (see Figure 3.4). We also study the spatial distribution of the Splash by splitting our solar neighbourhood sample into bins of vertical heights and radial distances and calculating the ratio of Splash to the disc, the Splash fraction. We adopt a slightly different selection for the solar neighbourhood in order to enable us to make a more direct comparison with the simulations. We find that the Splash fraction is larger at smaller radial distances and larger vertical heights. This same behaviour is seen across all of the ARTEMIS simulated galaxies we analyse, regardless of whether they are Sausaged or Sausageless (see Figures 3.14 & 3.15), showing that minor mergers also contribute to the Splash population in a similar way as a GE/S-like merger. We note here that this measurement is only taken in the solar neighbourhood and to form a full picture should be carried out across the whole galaxy. While this is possible for the simulations, we need to be cautious of any selection effects that may play a part when studying a sample in the MW.

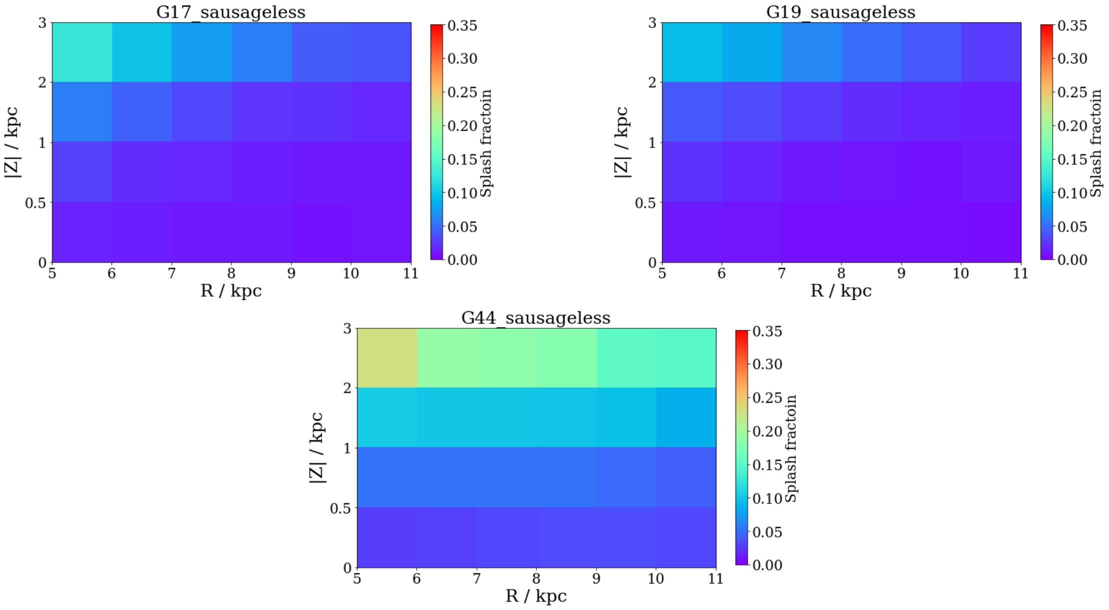

FIGURE 3.14: Same as Figure 3.6 but for Sausageless galaxies.

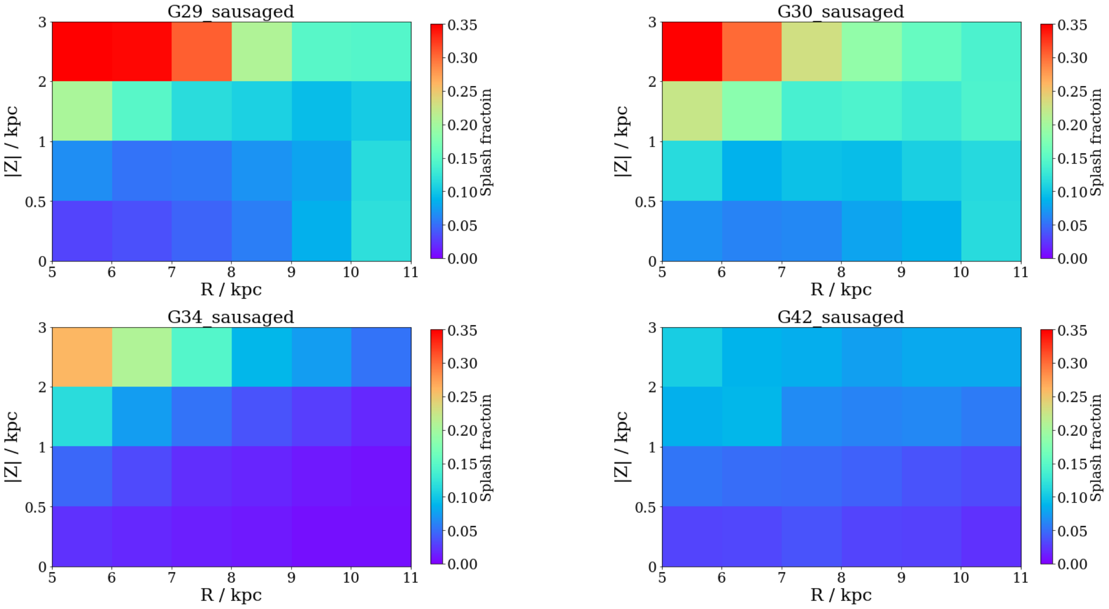

FIGURE 3.15: Same as Figure 3.6 but for Sausaged galaxies.

We compared in detail the chemical compositions of the Splash and high-α disc populations, as described in Section 3.3.2. The results, discussed in Section 3.4.1, reveal two populations that are statistically distinct from one another as is seen from the χ^2 and p-values on Figure 3.8. Moreover, we find chemical signatures that suggest the Splash is an older population. As a consistency check, we performed another test, described in Section 3.3.3. The results, presented in Section 3.4.2 uncover the elements that have the largest contribution to the differences we see in the first test. The elements that deviate by a large amount are shown in Figure 3.9. An examination of the distribution of Splash and high-α stars in the [X/Fe]-[Fe/H] plane for these elements is informative (Figure 3.7). For example, Al shows a small difference between the running median of the Splash and high-α disc, at most 0.05 dex, yet we still find that the two populations differ at a statistically significant level. This highlights the high degree to which we can carry out statistics for such a large set of high-precision data.

Though the chemistry of the Splash is significantly different from the rest of the high-α disc, as shown in Figures 3.8 & 3.9, there is a relatively smooth gradient for the α-abundances with respect to eccentricity (Figure 3.10) and angular momentum (top panel of Figure 3.12). This negative correlation is also seen for simulated galaxies that had both a GE/S-like merger and those that had only minor mergers (bottom panel of Figure 3.12). We only show two galaxies in this plot, one Sausaged and one Sausageless, but this correlation between [Mg/Fe] and Lz is seen for six of our simulated galaxies. The one galaxy that does not show much of a correlation, and has a more flat distribution, is G30 – a Sausaged galaxy. Further analysis of this galaxy is required to understand its Splash population. For the two galaxies that we show in Figure 3.12, we see a sharp decrease, a kink, just above Lz=0. This kink is seen in most of the simulated galaxies we analyse and could be an indication of the stars formed from the mixture of *in situ* and accreted gas.

We also perform a simple test to try and identify differences between our Sausaged and Sausageless galaxies by separating our galaxies into prograde and retrograde stars and calculating the ratio between the two. For the *in situ* stars, this would be the Splash fraction, and for the accreted stars it is the accreted retrograde fraction. By plotting the Splash fraction against the accreted retrograde fraction, shown in Figure 3.13, we find a strong positive correlation between the two. This plot is similar to Figures 10 and 16 from Grand et al. (2020) and Dillamore et al. (2022), respectively. Our plot shows the accreted retrograde ratio along the x-axis rather than the accreted ratio, which provides a tighter correlation with respect to the Splash fraction. This type of diagnostic can be used to infer the contribution of the Splash if we have an idea of the contribution from accreted stars in a galaxy, specifically those on retrograde orbits. There is, however, some scatter in this relation, as we can see from the distribution of G29, G42 and G44 in this plane. This scatter could be the result of multiple factors. A more in-depth analysis of the simulations is required to pinpoint the reason for the scatter here. An increased sample size would also allow us to see whether this scatter is significant. Here we provide a couple of hypotheses for what may be causing the scatter: 1) The length of time it takes for the merger to occur. A merger that takes a longer time would slow down the rate at which stars are splashed. 2) There could be *in situ* stars that were born in retrograde orbit even before a merger occurred. These stars would still be selected in our sample as Splash stars. Both of these hypotheses will be tested in our simulations in the near future.

From Figure 3.13 we also see that it is not only Sausaged galaxies that result in a large Splash fraction. G44, a Sausageless galaxy, has a higher Splash fraction than two of the Sausaged galaxies, G34 and G42. This suggests that for a Splash to form it is not necessary that the galaxy had undergone a GES-like merger. A Splash can be created as a result of minor mergers as well. The important factor, or at least one of the factors, for the amount of Splashed stars, is the amount of the accreted population that is in retrograde motion.

3.7 Summary

Our conclusions can be summarised as follows:

- We select a sample of high-α stars in the solar neighbourhood ($d_\odot < 3kpc$), which we split on the basis of their eccentricity. Stars with $e > 0.6$ are selected as our Splash population and the rest are the remaining high-α population.
- Looking at the velocities of the Splash compared to the rest of the Galactic solar neighbourhood, we find that the velocity distributions are as expected. The Splash is a low tangential velocity component with a more extended distribution in both the vertical and radial velocity components compared to the disc. We also examine the spatial distribution for the disc of the Galaxy, finding a larger contribution from the Splash at smaller radial and larger vertical distances from the Galactic centre. The ARTEMIS simulations are in qualitative agreement with these trends.
- Comparing the chemistry of the Splash to the rest of the high-α disc tells us that the two components are distinct at a statistically significant degree. When examining the individual elemental abundance ratios, we see that 12 of the 16 elements show significant differences. We later find that this is a result of comparing two opposite ends of a distribution.
- We split the high-α population into multiple eccentricity bins and look for correlations with abundance ratios. We find a correlation between the abundance ratios and eccentricity for most of the elements, especially the α abundances. The chemistry of each eccentricity bin is statistically distinct from all others. This highlights the correlation between chemistry and the kinematics of the Galaxy and how comparing kinematically selected populations can result in large chemical differences.

- We check for a signature of the Splash in the form of a discontinuity in the relation between chemistry and kinematics. In particular, we focus on the [Mg/Fe]-Lz plane of the 'high-α'. We identify a sharp decrease in [Mg/Fe] at Lz$\simeq$0. This kink is not seen in our MW sample. Interestingly, we see this kink and negative correlation in both Sausaged and Sausageless galaxies, with no clear difference between the two.

- The final diagnostic we explore is the comparison between the Splash fraction and accreted retrograde fraction for our simulated galaxies. We find that there is a strong positive correlation between these two measurements. We also see that Sausageless galaxies can have Splash fractions higher than Sausaged, suggesting that it is not only the high-mass accreted systems that can cause a Splash population, such as that defined in this chapter. The prograde or retrograde nature of the accreting satellite's orbit also plays a role in creating the Splash.

- Our findings show that the Splash is an extension of the high-α disc with no clear signature in the chemistry of the observational data for the Galaxy. We also find that regardless of whether a galaxy has undergone a GES-like merger a Splash population can still exist.

Chapter 4

Conclusions

In this thesis, I have presented novel results that provide an insight into the history of the Milky Way by analysing destroyed globular cluster members, N-rich stars, in the inner Galaxy (see Chapter 2) and a stellar population resulting from the heating of the early disk due to the merger of the GE/S, the Splash (see Chapter 3). In this chapter I bind together the findings from preceding chapters into a coherent picture of Milky Way substructures to give a better understanding towards the formation history of the Galaxy, drawing also from the body of literature discussed in Chapter 1 and the introductions and summaries of each of the other chapters.

One of the key results of this thesis is the evidence of an accreted population of N-rich stars located in the inner 4 kpc of the Galaxy. I find that about 30% of my inner Galaxy N-rich sample lies in the chemically accreted region of the [Si/Fe] - [Fe/H] plane. These accreted N-rich stars show significantly different kinematics compared to their *in situ* counterparts, supporting the evidence that they did not form *in situ* but more likely must have been accreted from dwarf satellites. Looking at the integrals of motions of the accreted N-rich population places them all in the region overlapping with the Heracles population (Horta et al., 2021a). I also find that the frequency of N-rich stars is an order of magnitude higher in the accreted region of the [Si/Fe] - [Fe/H] plane than the *in situ*. This result is at odds with numerical simulations shown in Hughes et al. (2020).

In Chapter 3 I present a chemodynamical analysis of the Splash population. My selection of the Splash is based on both chemistry and kinematics. In terms of spatial distribution, I show there is both a vertical and radial trend for the Splash fraction. The Splash fraction increases with larger vertical heights and smaller radial distances. I find the same trend in the simulated galaxies. I also show chemical comparisons between the Splash and the rest of the high-α disc using two methods that employ chi-square to statistically identify differences between elemental abundances. The coherent result obtained from both of these methods indicates that there is a distinct contrast in the chemical makeup between the Splash and high-α population with regards to their α-abundances. When testing to see if this difference between the Splash and high-α disc is simply due to an abundance gradient with respect to kinematics (here eccentricity), the results reveal a clear trend of increasing α-abundance with increasing eccentricity for the entire high-α disc sample. Looking at the `ARTEMIS` simulations, I find a similar trend for all galaxies. The trend follows that as [Mg/Fe] decreases, Lz increases. I observe this trend for both galaxy types, those with GE/S-like mergers and those without. When looking at the Splash fraction, I find Sausageless galaxies with higher Splash fractions than Sausaged galaxies. Such a result shows that a GE/S-like merger is not necessary to create a Splash, but rather a Splash can be caused by the merger of less massive mergers as well. I also find that the Splash fraction correlates strongly with the fraction of accreted stars on retrograde orbits, which implies that the orbital direction of the accreted system plays a role in creating a Splash.

Altogether, the results that I have presented in this thesis provide an insight into how studying the stellar populations of the Milky Way helps us towards a fuller picture of the Galaxy's assembly history. The idea that the chemistry of GCs can be used to identify an accreted population can also be used on other galaxies to study their formation history. In a similar sense, by looking at the Splash fraction of other galaxies, their accreted mass fraction can be constrained. This test could be applied to Andromeda where Gilbert et al. (2016) find evidence for Splash-like stars. By better understanding the assembly history of other galaxies we can compare them to the MW to figure out whether our Galaxy is unique and help answer the question: *do we live in a special place in the Universe?*

4.1 Future Works

Although these findings have provided more information about the stellar populations studied and the assembly history of the Milky Way, there are still questions for which answers are needed. The evidence of accreted N-rich stars raises the question of whether these stars in the inner Galaxy were already dissolved in their host galaxies before merging with the Milky Way or whether the GCs from which they originated were destroyed during or after the merger event. The question of whether accreted N-rich stars originate from the destruction of GCs in their host galaxies can be answered by searching for N-rich stars in the field of dwarf galaxies in the Local Group. This test would also provide insight into whether the conditions in dwarf galaxies are sufficient to destroy GCs. To make sure these tests can be carried out, a revision to the method for selecting N-rich stars in the fields of galaxies is required. Rather than only looking at the [N/Fe] abundance ratio, it would be more accurate to look at the correlations and anti-correlations in GCs to select the SG GC members. Such a method is being tested by O'Connor et al., in prep. Also, while I show that my chemical distinction between accreted an *in situ* maps on in a difference in kinematics, a better method to separate them may be available, especially at low metallicities where there is a lot of overlap in chemistry.

With regards to the Splash, a larger sample of simulated MW-like galaxies is what's really required to better understand the trends that I show in this Thesis. It is also important to look at the merger histories of those galaxies to be able to identify exactly what the Splash is, and how the Splash is created. This is something that can be done by looking at the different snapshots of the simulations to be able to time the events and then study the chemodynamics of the populations in a similar way to what I have done in this Thesis. Also, getting a larger sample of Splash stars in a larger area of the MW will provide a more galactic picture of how the Splash behaves in the MW. This can also be achieved by a full forward modelling of the survey data, using selection functions, in order to identify Splash stars more unambiguously.

This will all be possible with data from future *Gaia* mission and upcoming large-scale stellar surveys (SDSS-V Kollmeier et al. (2017); WEAVE Dalton et al. (2012); 4MOST de Jong et al. (2019); DESI DESI Collaboration et al. (2016); MOONS Gonzalez et al. (2020)). WEAVE is of particular interest, as I have provided the team with Splash stars as identified using APOGEE so that we can get an extended list of chemical abundances for the Splash that WEAVE will provide. In addition, improved simulation with larger samples of MW zoom-ins is crucial to understand exactly what we find from these observations.

Bibliography

Abdurro'uf et al., 2022, ApJS, 259, 35

Ahumada R., et al., 2020, ApJS, 249, 3

Amarante J. A. S., Beraldo e Silva L., Debattista V. P., Smith M. C., 2020, ApJ Letters, 891, L30

Andrews B. H., Weinberg D. H., Schönrich R., Johnson J. A., 2017, ApJ, 835, 224

Arentsen A., et al., 2020, MNRAS, 496, 4964

Athanassoula E., 2005, MNRAS, 358, 1477

Barbuy B., Chiappini C., Gerhard O., 2018, Annual Review of Astronomy and Astrophysics, 56, 223

Bastian N., Lardo C., 2018, Annual Review of Astronomy and Astrophysics, 56, 83

Beaton R. L., et al., 2021, AJ, 162, 302

Bekki K., 2019, MNRAS, 490, 4007

Belokurov V., Kravtsov A., 2022, MNRAS, 514, 689

Belokurov V., et al., 2006, ApJ Letters, 642, L137

Belokurov V., Erkal D., Evans N. W., Koposov S. E., Deason A. J., 2018, MNRAS, 478, 611

Belokurov V., Sanders J. L., Fattahi A., Smith M. C., Deason A. J., Evans N. W., Grand R. J. J., 2020, MNRAS, 494, 3880

Bennett M., Bovy J., 2019, MNRAS, 482, 1417

Binney J., Gerhard O., Spergel D., 1997, MNRAS, 288, 365

Bissantz N., Gerhard O., 2002, MNRAS, 330, 591

Bland-Hawthorn J., Gerhard O., 2016, Annual Review of Astronomy and Astrophysics, 54, 529

Blanton M. R., et al., 2017, AJ, 154, 28

Bonaca A., Conroy C., Wetzel A., Hopkins P. F., Kereš D., 2017, ApJ, 845, 101

Bovy J., 2015, ApJS, 216, 29

Bovy J., Rix H.-W., Liu C., Hogg D. W., Beers T. C., Lee Y. S., 2012, ApJ, 753, 148

Bovy J., Rix H.-W., Schlafly E. F., Nidever D. L., Holtzman J. A., Shetrone M., Beers T. C., 2016, ApJ, 823, 30

Bovy J., Leung H. W., Hunt J. A. S., Mackereth J. T., García-Hernández D. A., Roman-Lopes A., 2019, MNRAS, 490, 4740

Bowen I. S., Vaughan A. H. J., 1973, Appl. Opt., 12, 1430

Brook C. B., Kawata D., Gibson B. K., Flynn C., 2003, ApJ Letters, 585, L125

Bureau M., Aronica G., Athanassoula E., Dettmar R. J., Bosma A., Freeman K. C., 2006, MNRAS, 370, 753

Callingham T. M., Cautun M., Deason A. J., Frenk C. S., Grand R. J. J., Marinacci F., 2022, MNRAS, 513, 4107

Cao L., Mao S., Nataf D., Rattenbury N. J., Gould A., 2013, MNRAS, 434, 595

Carollo D., Martell S. L., Beers T. C., Freeman K. C., 2013, ApJ, 769, 87

Charbonnel C., Lagarde N., 2010, A&A, 522, A10

Ciucă I., et al., 2023, MNRAS,

Cooper A. P., Parry O. H., Lowing B., Cole S., Frenk C., 2015, MNRAS, 454, 3185

Crain R. A., et al., 2015, MNRAS, 450, 1937

Cui X.-Q., et al., 2012, Research in Astronomy and Astrophysics, 12, 1197

DESI Collaboration et al., 2016, arXiv e-prints, p. arXiv:1611.00036

Dalton G., et al., 2012, in McLean I. S., Ramsay S. K., Takami H., eds, Society of Photo-Optical Instrumentation Engineers (SPIE) Conference Series Vol. 8446, Ground-based and Airborne Instrumentation for Astronomy IV. p. 84460P, doi:10.1117/12.925950

Das P., Hawkins K., Jofré P., 2020, MNRAS, 493, 5195

Deason A. J., Belokurov V., Koposov S. E., Rockosi C. M., 2014, ApJ, 787, 30

Deason A. J., Fattahi A., Frenk C. S., Grand R. J. J., Oman K. A., Garrison-Kimmel S., Simpson C. M., Navarro J. F., 2020, MNRAS, 496, 3929

Debattista V. P., Mayer L., Carollo C. M., Moore B., Wadsley J., Quinn T., 2006, ApJ, 645, 209

Di Matteo P., Haywood M., Lehnert M. D., Katz D., Khoperskov S., Snaith O. N., Gómez A., Robichon N., 2019, A&A, 632, A4

Dillamore A. M., Belokurov V., Font A. S., McCarthy I. G., 2022, MNRAS, 513, 1867

Dillamore A. M., Belokurov V., Evans N. W., Davies E. Y., 2023, arXiv e-prints, p. arXiv:2303.00008

Drimmel R., 2000, A&A, 358, L13

Dwek E., et al., 1995, ApJ, 445, 716

Eggen O. J., Lynden-Bell D., Sandage A. R., 1962, ApJ, 136, 748

Eilers A.-C., Hogg D. W., Rix H.-W., Ness M. K., Price-Whelan A. M., Mészáros S., Nitschelm C., 2022, ApJ, 928, 23

Eisenstein D. J., et al., 2011, AJ, 142, 72

Elmegreen B. G., 2010, ApJ Letters, 712, L184

Fernandes L., et al., 2023, MNRAS, 519, 3611

Fernández-Trincado J. G., Beers T. C., Tang B., Moreno E., Pérez-Villegas A., Ortigoza-Urdaneta M., 2019, MNRAS, 488, 2864

Flynn C., Holmberg J., Portinari L., Fuchs B., Jahreiß H., 2006, MNRAS, 372, 1149

Font A. S., McCarthy I. G., Crain R. A., Theuns T., Schaye J., Wiersma R. P. C., Dalla Vecchia C., 2011, MNRAS, 416, 2802

Font A. S., et al., 2020, MNRAS, 498, 1765

Font A. S., McCarthy I. G., Belokurov V., 2021, MNRAS, 505, 783

Font A. S., McCarthy I. G., Belokurov V., Brown S. T., Stafford S. G., 2022, MNRAS, 511, 1544

Forbes D. A., 2020, MNRAS, 493, 847

Forbes D. A., Bridges T., 2010, MNRAS, 404, 1203

Freeman K., Bland-Hawthorn J., 2002, Annual Review of Astronomy and Astrophysics, 40, 487

Freudenreich H. T., 1998, ApJ, 492, 495

GRAVITY Collaboration et al., 2019, A&A, 625, L10

Gaia Collaboration et al., 2016, A&A, 595, A1

Gaia Collaboration et al., 2018, A&A, 616, A1

Gaia Collaboration et al., 2021, A&A, 649, A1

Gallart C., Bernard E. J., Brook C. B., Ruiz-Lara T., Cassisi S., Hill V., Monelli M., 2019, Nature Astronomy, 3, 932

García Pérez A. E., et al., 2016, AJ, 151, 144

Gerhard O., 2002, Social Science Research, 100, 129

Gilbert K. M., Beaton R., Dorman C., 2016, in Bragaglia A., Arnaboldi M., Rejkuba M., Romano D., eds, Vol. 317, The General Assembly of Galaxy Halos: Structure, Origin and Evolution. pp 134–139 (`arXiv:1603.05160`), doi:10.1017/S1743921315008479

Girardi L., et al., 2010, ApJ, 724, 1030

Gnedin O. Y., 2001, Astronomical and Astrophysical Transactions, 20, 39

Gnedin O. Y., Ostriker J. P., Tremaine S., 2014, ApJ, 785, 71

Gonzalez O. A., et al., 2020, The Messenger, 180, 18

Grand R. J. J., et al., 2017, MNRAS, 467, 179

Grand R. J. J., et al., 2018, MNRAS, 481, 1726

Grand R. J. J., et al., 2020, MNRAS, 497, 1603

Graur O., et al., 2014, ApJ, 783, 28

Gunn J. E., et al., 2006, AJ, 131, 2332

Hanke M., Koch A., Prudil Z., Grebel E. K., Bastian U., 2020, A&A, 637, A98

Harris W. E., 2010, arXiv e-prints, p. arXiv:1012.3224

Hasselquist S., et al., 2020, ApJ, 901, 109

Hasselquist S., et al., 2021, ApJ, 923, 172

Hawkins K., Jofré P., Masseron T., Gilmore G., 2015, MNRAS, 453, 758

Hayden M. R., et al., 2015, ApJ, 808, 132

Hayes C. R., et al., 2018, ApJ, 852, 49

Haywood M., Di Matteo P., Lehnert M. D., Snaith O., Khoperskov S., Gómez A., 2018, ApJ, 863, 113

Helmi A., 2020, Annual Review of Astronomy and Astrophysics, 58, 205

Helmi A., White S. D. M., de Zeeuw P. T., Zhao H., 1999, Nature, 402, 53

Helmi A., Babusiaux C., Koppelman H. H., Massari D., Veljanoski J., Brown A. G. A., 2018, Nature, 563, 85

Holtzman J. A., et al., 2015, AJ, 150, 148

Holtzman J. A., et al., 2018, AJ, 156, 125

Horta D., et al., 2020, MNRAS, 493, 3363

Horta D., et al., 2021a, MNRAS, 500, 1385

Horta D., et al., 2021b, MNRAS, 500, 5462

Horta D., et al., 2023, MNRAS, 520, 5671

Hubble E. P., 1926, ApJ, 64, 321

Hughes M. E., Pfeffer J. L., Martig M., Reina-Campos M., Bastian N., Crain R. A., Kruijssen J. M. D., 2020, MNRAS, 491, 4012

Ibata R. A., Gilmore G., Irwin M. J., 1994, Nature, 370, 194

Ibata R. A., Lewis G. F., Martin N. F., 2016, ApJ, 819, 1

Iwamoto K., Brachwitz F., Nomoto K., Kishimoto N., Umeda H., Hix W. R., Thielemann F.-K., 1999, ApJS, 125, 439

Jönsson H., et al., 2018, AJ, 156, 126

Jönsson H., et al., 2020, AJ, 160, 120

Jurić M., et al., 2008, ApJ, 673, 864

Karakas A. I., 2010, MNRAS, 403, 1413

Koch A., Grebel E. K., Martell S. L., 2019, A&A, 625, A75

Kollmeier J. A., et al., 2017, arXiv e-prints, p. arXiv:1711.03234

Koppelman H. H., Helmi A., Massari D., Price-Whelan A. M., Starkenburg T. K., 2019, A&A, 631, L9

Kruijssen J. M. D., 2014, Classical and Quantum Gravity, 31, 244006

Kruijssen J. M. D., 2015, MNRAS, 454, 1658

Kruijssen J. M. D., Pelupessy F. I., Lamers H. J. G. L. M., Portegies Zwart S. F., Icke V., 2011, MNRAS, 414, 1339

Kruijssen J. M. D., Maschberger T., Moeckel N., Clarke C. J., Bastian N., Bonnell I. A., 2012, MNRAS, 419, 841

Kruijssen J. M. D., Pfeffer J. L., Reina-Campos M., Crain R. A., Bastian N., 2019, MNRAS, 486, 3180

Kruijssen J. M. D., et al., 2020, MNRAS, 498, 2472

Lane J. M. M., Bovy J., Mackereth J. T., 2022, MNRAS, 510, 5119

Leaman R., VandenBerg D. A., Mendel J. T., 2013, MNRAS, 436, 122

Lee A., Lee Y. S., Kim Y. K., Beers T. C., An D., 2023, ApJ, 945, 56

Leung H. W., Bovy J., 2019a, MNRAS, 483, 3255

Leung H. W., Bovy J., 2019b, MNRAS, 489, 2079

Lind K., et al., 2015, A&A, 575, L12

López-Corredoira M., Cabrera-Lavers A., Gerhard O. E., 2005, A&A, 439, 107

Mackereth J. T., Bovy J., 2018, PASA, 130, 114501

Mackereth J. T., et al., 2017, MNRAS, 471, 3057

Mackereth J. T., Crain R. A., Schiavon R. P., Schaye J., Theuns T., Schaller M., 2018, MNRAS, 477, 5072

Mackereth J. T., et al., 2019, MNRAS, 482, 3426

Majewski S. R., et al., 2017, AJ, 154, 94

Marín-Franch A., et al., 2009, ApJ, 694, 1498

Martell S. L., Grebel E. K., 2010, A&A, 519, A14

Martell S. L., et al., 2016, ApJ, 825, 146

Martig M., et al., 2016, MNRAS, 456, 3655

Martin N. F., et al., 2022, MNRAS, 516, 5331

Massari D., et al., 2017, MNRAS, 468, 1249

Massari D., Koppelman H. H., Helmi A., 2019, A&A, 630, L4

Masseron T., et al., 2019, A&A, 622, A191

Masseron T., García-Hernández D. A., Santoveña R., Manchado A., Zamora O., Manteiga M., Dafonte C., 2020a, Nature Communications, 11, 3759

Masseron T., García-Hernández D. A., Zamora O., Manchado A., 2020b, ApJ Letters, 904, L1

McAlpine S., et al., 2016, Astronomy and Computing, 15, 72

McCarthy I. G., Font A. S., Crain R. A., Deason A. J., Schaye J., Theuns T., 2012, MNRAS, 420, 2245

McMillan P. J., 2011, MNRAS, 414, 2446

McMillan P. J., 2017, MNRAS, 465, 76

Mészáros S., et al., 2015, AJ, 149, 153

Mészáros S., et al., 2020, MNRAS, 492, 1641

Mutch S. J., Croton D. J., Poole G. B., 2011, ApJ, 736, 84

Myeong G. C., Vasiliev E., Iorio G., Evans N. W., Belokurov V., 2019, MNRAS, 488, 1235

Naidu R. P., Conroy C., Bonaca A., Johnson B. D., Ting Y.-S., Caldwell N., Zaritsky D., Cargile P. A., 2020, ApJ, 901, 48

Nataf D. M., 2017, PASA, 34, e041

Nataf D. M., et al., 2015, MNRAS, 447, 1535

Nataf D. M., et al., 2019, AJ, 158, 14

Ness M., et al., 2013, MNRAS, 430, 836

Nidever D. L., et al., 2015, AJ, 150, 173

Norris J. E., Yong D., Venn K. A., Gilmore G., Casagrande L., Dotter A., 2017, ApJS, 230, 28

Odenkirchen M., et al., 2003, AJ, 126, 2385

Pfeffer J., Bastian N., Kruijssen J. M. D., Reina-Campos M., Crain R. A., Usher C., 2019, MNRAS, 490, 1714

Pfeffer J. L., Trujillo-Gomez S., Kruijssen J. M. D., Crain R. A., Hughes M. E., Reina-Campos M., Bastian N., 2020, MNRAS, 499, 4863

Phillips S. G., et al., 2022, MNRAS, 510, 3727

Portail M., Gerhard O., Wegg C., Ness M., 2017, MNRAS, 465, 1621

Portinari L., Chiosi C., Bressan A., 1998, A&A, 334, 505

Queiroz A. B. A., et al., 2021, A&A, 656, A156

Rattenbury N. J., Mao S., Sumi T., Smith M. C., 2007, MNRAS, 378, 1064

Reina-Campos M., Hughes M. E., Kruijssen J. M. D., Pfeffer J. L., Bastian N., Crain R. A., Koch A., Grebel E. K., 2020, MNRAS, 493, 3422

Renzini A., 2008, MNRAS, 391, 354

Renzini A., Voli M., 1981a, A&A, 94, 175

Renzini A., Voli M., 1981b, A&A, 500, 221

Robin A. C., Marshall D. J., Schultheis M., Reylé C., 2012, A&A, 538, A106

Robin A. C., Reylé C., Fliri J., Czekaj M., Robert C. P., Martins A. M. M., 2014, A&A, 569, A13

Salaris M., Weiss A., 2002, A&A, 388, 492

Sanders J. L., Smith L., Evans N. W., 2019, MNRAS, 488, 4552

Santana F. A., et al., 2021, AJ, 162, 303

Savino A., Posti L., 2019, A&A, 624, L9

Schaye J., et al., 2015, MNRAS, 446, 521

Schiavon R. P., et al., 2017a, MNRAS, 465, 501

Schiavon R. P., et al., 2017b, MNRAS, 466, 1010

Schiavon R. P., Mackereth J. T., Pfeffer J., Crain R. A., Bovy J., 2020, in Bragaglia A., Davies M., Sills A., Vesperini E., eds, Proceedings of the International Astronomical Union Vol. 351, Star Clusters: From the Milky Way to the Early Universe. pp 170–173 (`arXiv:2002.08380`), doi:10.1017/S1743921319007889

Searle L., Zinn R., 1978, ApJ, 225, 357

Shetrone M., et al., 2015, ApJS, 221, 24

Siess L., 2010, A&A, 512, A10

Skrutskie M. F., et al., 2006, AJ, 131, 1163

Smith V. V., et al., 2021, AJ, 161, 254

Springel V., 2005, MNRAS, 364, 1105

Stanek K. Z., Udalski A., SzymaŃski M., KaŁuŻny J., Kubiak Z. M., Mateo M., KrzemiŃski W., 1997, ApJ, 477, 163

Starkenburg E., Oman K. A., Navarro J. F., Crain R. A., Fattahi A., Frenk C. S., Sawala T., Schaye J., 2017, MNRAS, 465, 2212

Tang B., Liu C., Fernández-Trincado J. G., Geisler D., Shi J., Zamora O., Worthey G., Moreno E., 2019, ApJ, 871, 58

Tang B., Fernández-Trincado J. G., Liu C., Yu J., Yan H., Gao Q., Shi J., Geisler D., 2020, ApJ, 891, 28

Taylor D. J., et al., 2022, MNRAS, 513, 3429

Tolstoy E., Hill V., Tosi M., 2009, Annual Review of Astronomy and Astrophysics, 47, 371

Tremaine S. D., Ostriker J. P., Spitzer L. J., 1975, ApJ, 196, 407

Tumlinson J., 2010, ApJ, 708, 1398

Venn K. A., Irwin M., Shetrone M. D., Tout C. A., Hill V., Tolstoy E., 2004, AJ, 128, 1177

Ventura P., Di Criscienzo M., Carini R., D'Antona F., 2013, MNRAS, 431, 3642

Wegg C., Gerhard O., 2013, MNRAS, 435, 1874

Weiland J. L., et al., 1994, ApJ Letters, 425, L81

Weinberg D. H., et al., 2022, ApJS, 260, 32

White S. D. M., Rees M. J., 1978, MNRAS, 183, 341

Wiersma R. P. C., Schaye J., Theuns T., Dalla Vecchia C., Tornatore L., 2009, MNRAS, 399, 574

Wilson J. C., et al., 2019, PASA, 131, 055001

Xiang M., Rix H.-W., 2022, Nature, 603, 599

Yanny B., et al., 2009, AJ, 137, 4377

Youakim K., et al., 2020, MNRAS, 492, 4986

Zamora O., et al., 2015, AJ, 149, 181

Zasowski G., et al., 2017, AJ, 154, 198

Zhao G., Zhao Y.-H., Chu Y.-Q., Jing Y.-P., Deng L.-C., 2012, Research in Astronomy and Astrophysics, 12, 723

de Jong R. S., et al., 2019, The Messenger, 175, 3

de los Reyes M. A. C., Kirby E. N., Ji A. P., Nuñez E. H., 2022, ApJ, 925, 66